



מכון ויצמן למדע

WEIZMANN INSTITUTE OF SCIENCE

Thesis for the degree

Master of Science

Submitted to the Scientific Council of the
Weizmann Institute of Science
Rehovot, Israel

עבודת גמר (תזה) לתואר

מוסמך למדעים

מוגשת למועצה המדעית של
מכון ויצמן למדע
רחובות, ישראל

By

Adam Rubin

מאת

אדם רובין

חקר גלאי קרינה מסוג THGEM:
אסימטריה בתהליך ההכפלה ותפעול עם
אלקטרודות עם התנגדות גבוהה

THGEM-detector investigations:
electron-avalanche asymmetry and
operation with resistive anodes

Advisor:

Prof. Amos Breskin

March 2013

מנחה:

פרופ. עמוס ברסקין

ניסן תשע"ג

Abstract

The Thick Gas Electron Multiplier (THGEM) was developed at the Weizmann group in 2004. It is a simple device, in which radiation-induced electrons are multiplied in millimeter-scale holes drilled in a printed-board circuit. THGEMs have been studied extensively, becoming a basic detector element in numerous applications. Like many other gas-avalanche detectors, occasional discharges limit the dynamic range of THGEM-based detectors. In this thesis I report on two investigations that were carried out: on the one hand, trying to understand some potential origins of discharges and on the other, trying to expand the dynamic range of these multipliers. My research focused on the study of avalanche formation inside THGEM holes and on coupling THGEM electrodes to readout anodes of high bulk resistivity. I found that although the avalanche develops asymmetrically inside the hole, it does not develop on its circumference; therefore it should not be prone to surface defects. I also found that highly resistive anode materials can be good candidates for increasing the dynamic range of THGEM detectors.

Acknowledgments

I would like to express my deep appreciation to my colleagues who assisted, encouraged and advised me in my research.

Thank you to Prof. Amos Breskin, who shared his vast knowledge of detection physics and allowed me to explore on my own, make mistakes, and learn from them. The opportunities he has given me for research, schools and experiments are invaluable.

To Dr. Lior Arazi and Dr. Shikma Bressler, who lent me their ears and were always willing to discuss and think together about our pressing problems.

To Dr. David Vartsky who supported my research with equipment, his experience, and his gentle manner.

To my friends from the lab: Luca, Michael, Artur and Itamar who helped and encouraged.

To Moshe Klin, his technical knowledge and warm personality made working in the lab a pleasure.

To Nachum Zwang, who was always available for a hallway discussions.

To Yehuda Asher, an expert craftsman.

To Dana, who made this all possible.

Thank you.

Table of Contents

1	Introduction	1
2	The Thick-GEM	2
3	The physics of radiation detection—a concise review	5
3.1	Energy deposition of radiation in matter	5
3.2	Charge transport and diffusion in the medium	7
3.3	Excitation and avalanche formation	8
4	Optical recording of avalanches in THGEM holes	11
4.1	Introduction	11
4.2	Experimental Setup & Methodology	13
4.2.1	Detector Setup	13
4.2.2	Optical setup	14
4.2.3	Description of the assays	16
4.3	Results	20
4.3.1	Hole multiplicity for different detector configurations	20
4.3.2	Scan across hole with a collimated x-ray beam	21
4.3.3	High statistics runs and simulations	23
4.4	Discussion on the optical recording of avalanches	24
5	Investigations of Resistive-Plate WELL (RPWELL)	27
5.1	Introduction	27
5.2	Experimental setup and methodology	32
5.2.1	Electrode preparation and characteristics	32
5.2.2	Assays	34
5.3	Results	37
5.3.1	Pulse shapes and gain curves	37
5.3.2	Exposure to high primary charge	39
5.3.3	Rate dependence	41

5.4	Discussion on the resistive-anode investigations	41
6	Summary.....	45
7	References	47

1 Introduction

Micropattern gas-avalanche detectors (MPGD) are currently at the forefront of radiation detection. Among the leading technologies are: the Gas Electron Multiplier (GEM) [1], MICROMEGAS [2], and the Thick-GEM (THGEM) [3]. They are being thoroughly investigated, and are used in several major high energy physics and nuclear physics experiments. The Weizmann Radiation Detection Lab participates in this major R&D effort, within the CERN-RD51 project. MPGDs, due to their fine electrode structures, perform better than classical wire chambers in terms of counting-rates capability, time-resolution and spatial resolution.

Typical applications of MPGDs involve amplifying small signals in the midst of high background. For minimally ionizing particle (MIP) applications, the primary charge deposited in the detector is of the order of a few tens of electrons, while in UV-photon detectors of Ring Imaging CHerenkov (RICH) applications, where the gaseous multiplier is coupled to a photocathode, the initial signal is only a single photoelectron. Therefore, according to the application, gains spanning between $\sim 5 \times 10^3$ and $\sim 10^5$ are necessary for efficient detection, respectively. These small signals must be measured in the presence of unwanted highly ionizing particle (HIP) background, such as neutron recoils and nuclear fragments [4–6]. These deposit energy one or two orders of magnitude higher than the expected signal: often causing discharges that can damage the detector and its electronics. Some gaseous detectors, such as wire chambers (section 3.3) and resistive plate chambers (section 5) are able to saturate intense signals, i.e. have a limited response without breakdown; however avalanche-saturation modes in MPGDs are still elusive, and the onset of discharges sets an upper limit on the maximal achievable gain of these detectors (e.g. $\sim 10^6$ gain for single electrons) [7].

A fundamental problem of the MPGD community is therefore to develop sensitive, fast and reliable detectors, robust also in the presence of highly ionizing background. Some attempts have been made to develop detectors equipped with resistive electrodes, damping HIP-induced discharges (as discussed below). Promising results were reached for example with resistive-MICROMEGAS detectors [8], recently selected as part of the CERN-ATLAS muon tracking system upgrade (section 5). Another important advance is our Weizmann Institute group's Segmented Resistive WELL (SRWELL, section 2); it is a hole-multiplier, from the THGEM family, that has performed successfully in a recent pion-beam test at CERN.

Operation at higher than currently achievable gains and radiation rates is paramount to the selection of MPGDs for radiation detection in the next generation of high energy physics experiments and other fields.

This thesis describes work conducted to enhance the dynamic range of THGEM-like detectors from two different perspectives. The first study was on the fundamentals of avalanche formation inside the THGEM holes. We set up an optical readout system and recorded the photons emitted by the electron-avalanche; we studied the asymmetry of the avalanche development inside the holes in different multiplier geometries, scanning the detector with a narrow x-ray beam and recording avalanche position with an intensified CCD camera. We also measured the hole-multiplicity (the number of holes activated by a single x-ray conversion) for different detector configurations.

The second study involved coupling a single-faced THGEM to highly resistive anodes and recording the induced charge. This was a continuation of the Weizmann Institute group's work on the SRWELL. In the SRWELL, layers with surface resistivity on the order of 1-20 M Ω /square mitigated discharges: successfully reducing their intensity by roughly one order of magnitude [9]. In this work layers with high bulk resistivity ($\sim 10^9$ - 10^{12} Ω cm) were explored. We show spectra, pulse shapes, gain curves and the rate dependence of the gain for several materials investigated.

2 The Thick-GEM

The two studies presented in this thesis were conducted on THGEM detectors. The THGEM is an electron multiplier—developed at the Weizmann Institute detector-physics group—in which avalanche multiplication develops within sub-millimeter diameter holes, mechanically drilled in a standard two-sided copper-clad printed circuit board (Figure 1); it is manufactured from common materials including FR4, G-10 and Kevlar. Radiation-induced electrons resulting of gas ionization, or originating from radiation converters deposited on the THGEM electrode surface (e.g. a photocathode) [10] are focused into the holes. The high electric field set by the potential difference between the THGEM faces induces avalanche multiplication within the holes. Very large gains, exceeding 10^6 , can be reached by cascading a few THGEM elements as reviewed in [10]. The position of interaction can be derived from avalanche localization, typically by recording charges induced on a patterned anode coupled to the last multiplier in the cascade [11] or by optical readout [12].

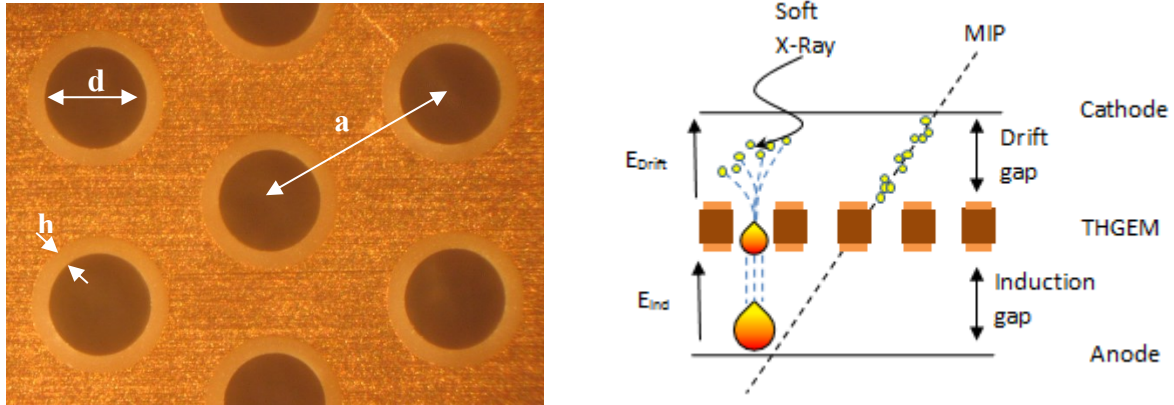


Figure 1: Microscope image of a THGEM electrode, of a thickness t (left) and an illustration of a typical THGEM detector configuration (not to scale), showing x-ray and minimally ionizing particles interactions (right).

Figure 2 shows the THGEM's dipole-shaped field, resulting from a potential difference applied between its two faces. This field can reach tens of kV/cm—well over the threshold of electron multiplication in a noble gas such as neon. Figure 2 also shows that the field has a saddle shape: the field at the center of the hole is maximal going along the axis and minimal going perpendicular to the axis. This was observed in [13] and implies that there is increased multiplication near the edges of the hole. This is important for a number of reasons: first, the glass fibers in FR4 often jut out of the material where the drilling occurs, creating sharp points where charging up can potentially cause electrical breakdown. Second, the dielectric material increases the nearby field and may encourage surface streamers [14]. Surface streamers are avalanches that can self-propagate due to the dielectric material next to them (see section 4.1 for an expanded description).

Early works explored the use of THGEMs as UV photo-sensors for Ring Imaging CHerenkov (RICH) detectors [10]. THGEM's large surface area makes them an excellent substrate onto which a photocathode (e.g. CsI) can be deposited. The geometry hides the deposited photocathode from the avalanche-induced secondary photons: efficiently preventing secondary avalanches from occurring. Ultraviolet photons impinging on the photocathode surface cause the emission of electrons, collected efficiently [15] into and multiplied in the THGEM holes. High charge gains are reached by cascading several THGEM elements, as presently applied in the UV sensors for the RICH detectors of CERN-COMPASS [16]. Following the success of room-temperature UV detectors, cryogenic THGEM UV detectors with CsI coatings were proposed as gaseous photomultipliers to detect liquid xenon scintillation in medical imaging and dark matter searches [17,18].

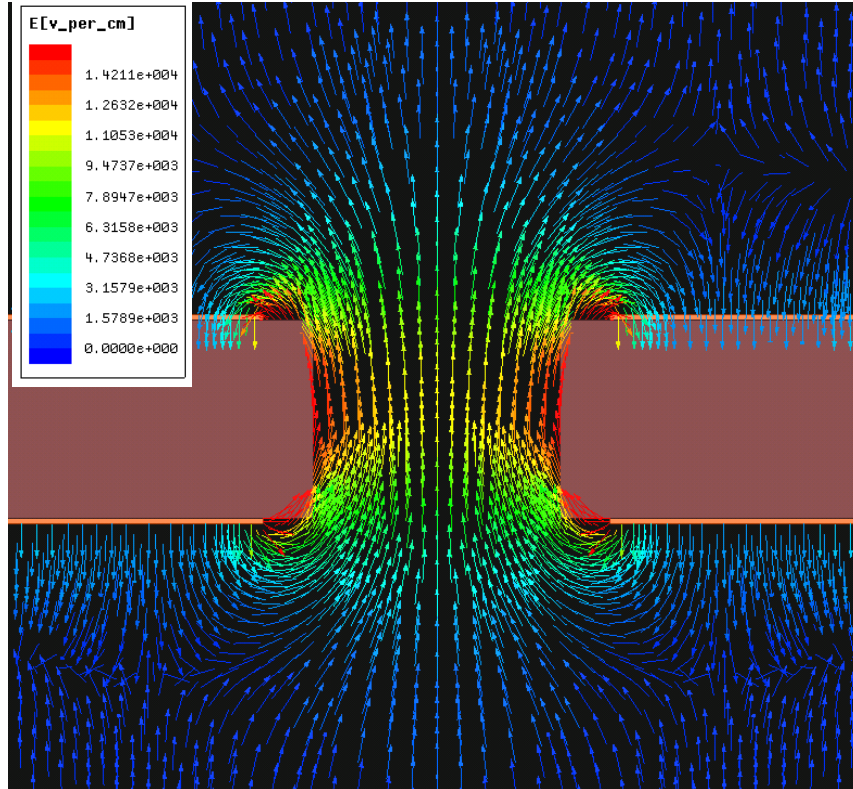


Figure 2: Electric field for a 0.4mm thick THGEM having parameters (see Figure 1): $a=1, d=0.5, h=0.1$ mm; the THGEM is preceded and followed by 5mm drift and induction gaps, respectively. Voltages were set to Cathode=-1300V, Top=-1050V, Bottom=-250V, Anode=0V. The fields were simulated using ANSYS Maxwell [19]. The field strength has a saddle shape with a high-field concentration close to the hole circumference: at the walls and at the edges.

THGEMs have also been investigated for x-ray imaging applications. Cortesi et al. [11] obtained a point spread function of 0.7mm FWHM with a double-THGEM of hole-pitch 1mm and a readout anode with strips 2mm apart. They also found the gain to be uniform to within 10% for a $10 \times 10 \text{mm}^2$ double THGEM structure. Another ongoing application is that of fast-neutron imaging as reviewed in [20]; new ideas of THGEM neutron detectors coupled to efficient multi-foil converters are described in [21].

Finally, the Weizmann Institute group—in collaboration with two Portuguese groups from Universidade de Aveiro and Universidade de Coimbra—demonstrated that THGEMs are strong candidates for the Digital Hadronic Calorimeter (DHCAL [22]) at the planned International Linear Collider (ILC). Several beam tests were performed [23], in which I participated, most recently in November 2012 with yet to be published results [24,25]. The requirements of DHCAL are thin sampling detectors, with $1 \times 1 \text{cm}^2$ pads, operated in digital mode, with high efficiency and low pad multiplicity. For this purpose a Segmented Resistive WELL (SRWELL), previously referred to as Gridded Resistive WELL (GRWELL) [9]. The SRWELL is a single-faced THGEM coupled to a $\sim 1\text{-}20 \text{M}\Omega/\text{square}$ resistive layer segmented

into $1 \times 1 \text{ cm}^2$ pads by a copper grid (to prevent large diffusion of the charge). In a recent beam test, the SRWELL gave efficiencies $>95\%$ and pad-multiplicities <1.2 , making it a strong competitive candidate for future DHCAL applications.

3 The physics of radiation detection—a concise review

3.1 Energy deposition of radiation in matter

A typical application of gas-avalanche detectors is the detection of Minimally Ionizing Particles (MIPs). Charged particles traversing a gas lose energy through electromagnetic interaction. The stopping power is given by the Bethe-Bloch equation [26]:

$$\frac{dE}{dX} = -K \frac{Z}{A} \frac{\rho}{\beta^2} \left\{ \log \frac{2mc^2 \beta^2 E_M}{I^2 (1 - \beta^2)} - 2\beta^2 \right\}, K = \frac{2\pi N z^2 e^4}{mc^2}, \quad (1)$$

where:

- N is the Avogadro number
- m and e are the electron mass and charge
- Z and A are the atomic number and mass
- ρ is the density of the medium
- I is the effective ionization potential of the medium
- E_M is the maximal energy transfer
- β is the dimensionless velocity (v/c)
- z is the charge

At a high enough velocity the stopping power becomes constant: in this region all massive charged particles are “minimally ionizing”. Typical values of energy deposition for MIPs in neon and argon are 1.41 keV/cm and 2.44 keV/cm respectively at normal conditions [26]. The number of created electron-ion pairs is calculated with W_i : the average energy to create such pair; its experimental value in neon is $W_i \approx 36 \text{ eV/pair}$ and in argon $W_i \approx 26 \text{ eV/pair}$ [26]. Conversion gaps in gas-avalanche detectors can be as small as a few millimeters, indicating that the primary deposited charge is usually on the order of several tens of electrons.

Radioactive sources are convenient for detector research and development. Soft x-rays in the keV range are particularly useful: producing hundreds of electrons when interacting with a noble gas such as neon or argon. ^{55}Fe is a commonly used source, emitting 5.9 keV x-rays.

Alternatively, x-ray tubes emit photons with energy equal to the target's K_α line (in addition to Bremsstrahlung radiation); for copper this is $\sim 8\text{keV}$. Photons in this energy range primarily interact with gas by photoelectric absorption, with a cross section (Figure 3) that is roughly two orders of magnitude larger than that of Compton scattering. One difficulty in relating results from x-rays to minimally ionizing particles is the long range the photoelectron has in the gas. In neon the range of an 8keV electron is typically $\sim 1.8\text{mm}$. Figure 4 shows a simulation of an electron track in $\text{Ne}/5\%\text{CF}_4$ (used in this work) at normal temperature and pressure using HEED [27]. HEED is a program, interfaced with Garfield [28], for simulating the interaction of fast charged particles in gas mixtures and their ionization paths. An approximation for the practical range R_p in g cm^{-2} is given by

$$R_p = 0.71E^{1.72}$$

where E is in MeV [26]. The electron range has implications for x-ray imaging as well: a large range will degrade the imaging resolution; therefore tailoring the gas and pressure to the application is of utmost importance. For example, the photoelectron range in argon is a factor of two smaller than that of neon. The imaging potential of THGEMs in both argon [11] and neon [29] has been investigated by the Weizmann group.

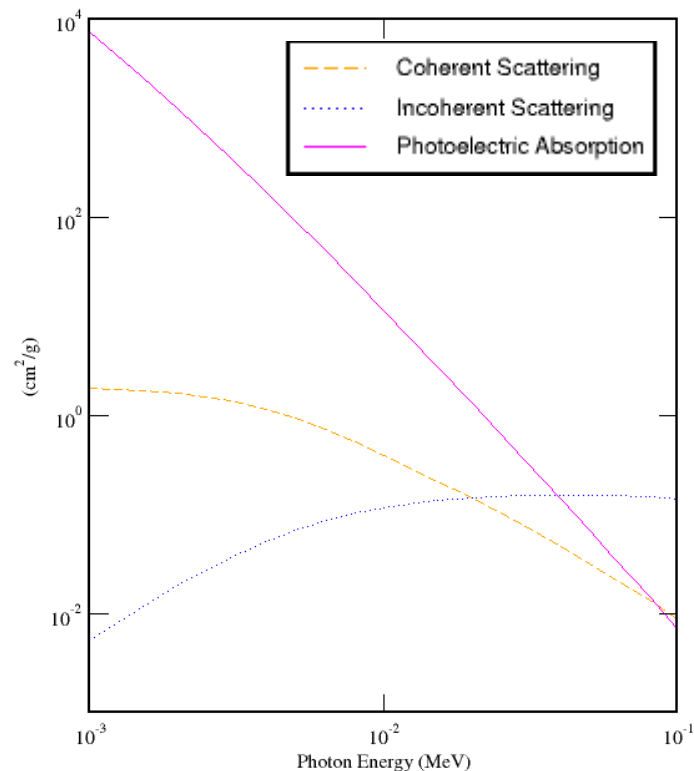


Figure 3: Photon cross sections in neon [30].

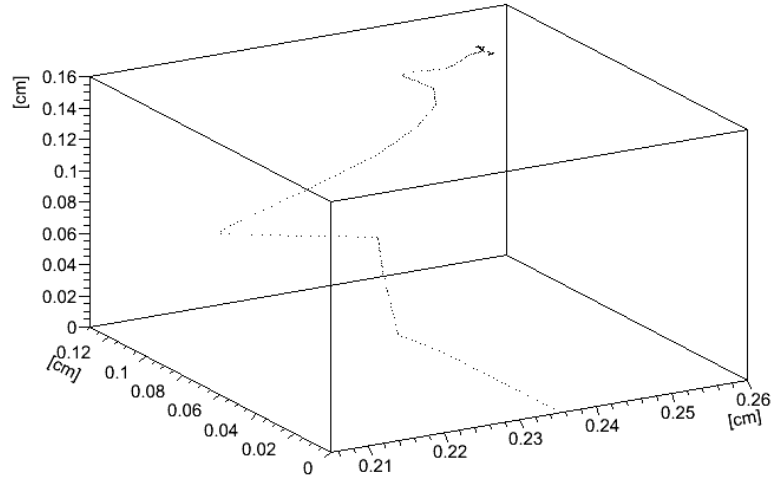


Figure 4: HEED simulation of 8keV photoelectron track in Ne/5%CF₄ at normal temperature and pressure. Each point is the position of an electron-ion pair created. Track origin is at (0,0,0.236) cm.

The interaction of photons with the medium also attenuates the incident radiation. The intensity follows

$$I = I_0 e^{-x/\lambda}, \quad (2)$$

where I is the intensity, I_0 is the initial intensity, x the length and $\lambda = (\mu\rho)^{-1}$ is the absorption mean free path, where μ is the mass attenuation coefficient and ρ is the density. For neon and argon, the absorption mean free path is 50cm and 5cm respectively at normal temperature and pressure [31]. For a 1cm gas gap, the photoelectric interactions occur uniformly throughout the gap in neon (2% difference), but occur 20% more at the beginning than at the end of the gap in argon.

3.2 Charge transport and diffusion in the medium

The ion mobility in a medium is defined as

$$w^+ = \mu^+ E \quad (3)$$

where w^+ is the ion drift velocity, μ^+ is the ion mobility and E is the electric field. Typical ion mobilities are on the order of $1\text{cm}^2\text{V}^{-1}\text{sec}^{-1}$. This translates to drift velocities of $5 \times 10^2 \text{cm/sec}$ at 0.5kV/cm . Electron drift velocity is 3 or 4 orders of magnitude higher but is typically a complicated function of the electric field (Figure 5), making the definition of a mobility inconvenient. This is due to the electron's low mass and varying cross section for elastic and inelastic scattering [32]. Typical electron velocities are on the order of $\sim 10^7 \text{cm/s}$. In neon at 0.5kV/cm and NTP, electrons and ion traverse a 10mm gap in $\sim 140\text{ns}$ and $\sim 2\text{ms}$ respectively.

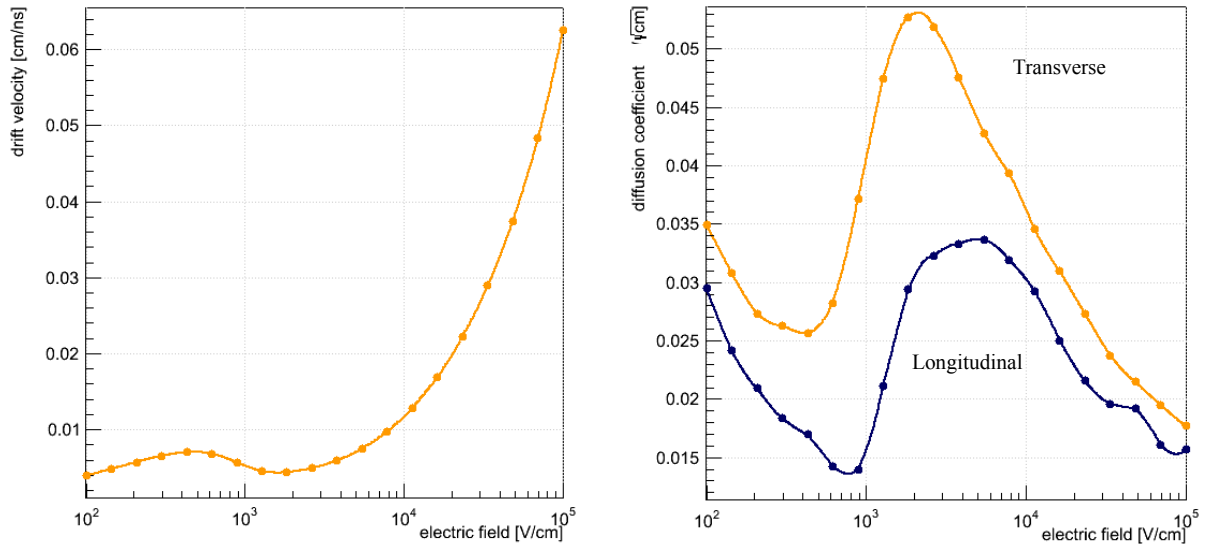


Figure 5: Drift velocity (left) and diffusion coefficients¹ (right) of electrons in Ne/5%CF₄. Calculated with MagBoltz [33].

In addition to the linear movement of the charged carriers, diffusion has a strong effect on the spread of charge inside the medium. Generally charges in a medium will diffuse by a random walk, with their distribution following a Gaussian distribution. For a 10mm drift gap, the r.m.s of the transverse diffusion of electrons will be $\sim 260\mu\text{m}$.

3.3 Excitation and avalanche formation

Charged particles interact with gas primarily through interaction with the atomic electrons; therefore an energetic charged particle will lose most of its energy to excited and ionized atomic or molecular states [34]. Some of the ejected primary electrons are energetic and cause ionization (liberating secondary electrons) and excitation. The de-excitation spectrum observed depends on the gas used, the pressure and the excitation mechanism. At low pressure the atoms decay radiatively, however under pressure (all of the work presented here was done under atmospheric pressure), collisions become important and complicated multi-body interactions affect the lifetime and spectrum of de-excitation. Excited atoms decay mostly by fluorescence emitting photons in the vacuum ultra violet (VUV). This is due to radiative de-excitation from the first excited states of the noble gas (for argon and neon these are 107nm and 74nm respectively). In addition to the VUV strong atomic lines, there are two continua at slightly higher wavelengths associated with di-atomic (excimer) transitions to the repulsive ground state. The visible and infrared features of the spectrum are atomic and are due to cascade transitions to the 1s state. Adding a gas such as Tetrakis dimethylamino ethylene (TMAE) [35] or CF₄ [36,37] can cause the mixture to strongly emit photons in the

¹ The r.m.s of the Gaussian distribution of charge can be calculated by multiplying the diffusion coefficient by \sqrt{g} , where g is the gap size in cm.

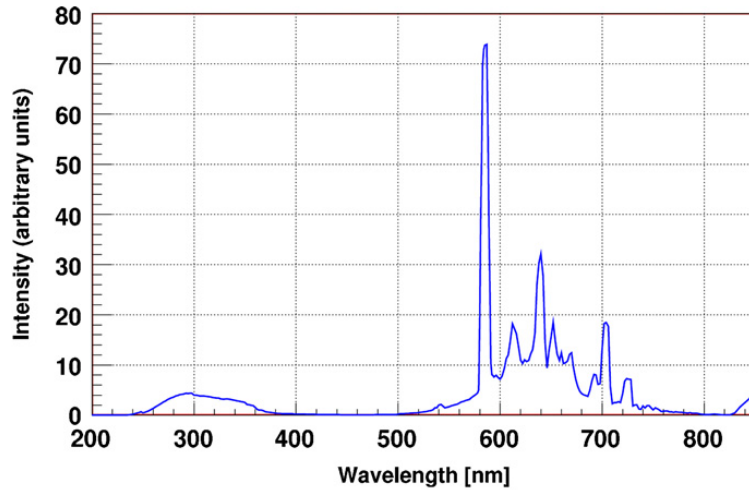


Figure 6: Secondary spectrum of 1 atmosphere Ne/10%CF₄ produced by a capillary plate at gain $\sim 10^4$. From [38].

visible spectrum (Figure 6) making them convenient for optical recording uses (see section 4.1). The mechanism responsible for visible emission in CF₄ (used in this thesis work) is an excited Rydberg state of CF₄ which decays to an emitting CF₃⁺ fragment [39].

In addition to the primary scintillation (from the initial interaction of the particle or photon with the gas), it is possible to induce secondary scintillation by accelerating the ionization electrons with electric fields. This was employed in the present work. Figure 7 shows the electron impact cross sections for neon. At fields on the order of ~ 1 kV/cm at NTP the electron begins to acquire enough energy to excite the noble gas atoms. At higher fields (~ 2.5 kV/cm in neon) ionization begins and quickly becomes the dominant process as the electric field is raised. In some applications, such as in noble-gas Time Projection Chambers (TPC) it is undesirable to cause ionization, therefore the electric field and pressure must be tailored so that the electrons will acquire enough energy to excite but not ionize the gas (this working point is called electroluminescence). These same processes are relevant during electron multiplication, and it is possible to obtain very high optical signals from electron avalanches; this was utilized in the presented work (see section 4).

Electrons multiplying in gas were studied by Townsend at the beginning of the 20th century [40]. The following model for avalanche formation is called a Townsend Avalanche and follows an exponential law

$$N(x) = e^{\alpha x} \quad (4)$$

where N is the number of electrons in the avalanche and α is the First Townsend Coefficient which represents the number of electron-ion pairs created per unit length in the direction of

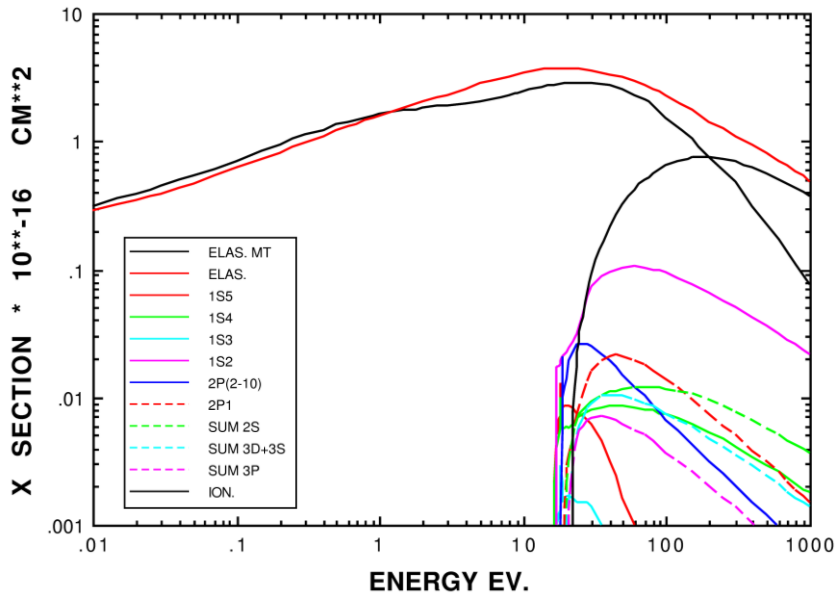


Figure 7: Electron impact cross sections for neon.

the field [32]. α is a difficult quantity to calculate, and typically it is found by numerical simulation. At high electric fields breakdown occurs.

Two types of breakdown exist: a slow mechanism due to successive avalanches called Townsend breakdown and a fast mechanism which induces breakdown in a single avalanche. Slow breakdown can be successfully modeled by adding feedback mechanisms that cause secondary avalanches: photon emission by excited states in the gas can liberate electrons from the cathode; positive ions can liberate electrons upon impact with the cathode; and far less likely—ion impact can ionize the gas atoms themselves. Each mechanism has a different timescale (with photon feedback being the fastest by several orders of magnitude); however, slow breakdown typically occurs over the course of $\sim 10^{-5}$ s. Photon feedback was found to be very efficiently suppressed [41] at small concentrations of gas quencher—complex molecules with rotational and vibrational modes such as CH_4 , CF_4 , and CO_2 —which have a wide absorption band and release the energy through collisions or by dissociation into simpler molecules. Ion backflow is an important process particularly for single photon applications of GPMs, and is sometimes dealt with by creating mechanical barriers for the ions, such as staggering THGEMs [42].

Fast breakdown occurs over the course of $\sim 10^{-8}$ s. The Townsend breakdown mechanism cannot explain two main features of fast breakdown. First the timescale is much too short to be explained by successive avalanches [32]. For example the electron velocity is $\sim 10\text{cm}/\mu\text{s}$, indicating that it would take $\sim 10^{-7}$ s to cross a 1cm gap, an order of magnitude longer than

what is observed. The second feature that is unexplained is the filamentary and branched nature of streamers. The Townsend mechanism fails primarily because it does not take into account the space charge of the avalanche itself. The charge concentration can be quite large: enough to cause self-propagation of the avalanche and subsequent breakdown. A rule of thumb due to Raether [43], the so called Raether limit, is that $\sim 10^6$ electrons in an avalanche will begin a streamer. Despite the above, streamers do not necessarily degrade to sparks.

In wire chambers several different saturation modes exist. The most famous is the Geiger-Müller mode, which is the basis of the Geiger counter developed in 1928 [44]. In this mode, the avalanche induces additional avalanches along the length of the wire, until the entire wire is covered. The discharge is terminated by the ion sheath surrounding the wire, which reduces the electric field and prevents further multiplication. In proportional chambers with thick wires and special gas mixtures (“magic gas” and others), a self-quenching streamer mode (SQS) is observed [45]. A streamer develops from the anode wire towards the cathode, but terminates due to the drop in electric field as the inverse of the distance from the wire. This mode extends only a few hundred microns along the wire (and a few mm from the wire), reducing the dead time and area. Sparks may also be limited by resistivity: if the outer circuit cannot supply the current to sustain the breakdown, the spark will rapidly decay. In all of the above, the signal is independent of the initial charge created in the medium, i.e. the term saturation modes.

4 Optical recording of avalanches in THGEM holes

4.1 Introduction

Peskov et al. [14], in work on Micro Strip Gas Counters (MSGCs, [46]), showed that the presence of dielectric materials increases the probability of breakdown due to increased electric field near the dielectric. It was suggested that if an avalanche-induced streamer forms near the dielectric surface, the electric field may be enhanced enough to cause a self-propagation of the streamer, leading to breakdown; this was called the “surface streamer” mechanism. In the case of the THGEM, the aforementioned saddle shape of the field motivated a study of the avalanche distribution within the hole. It was estimated from the shape of the field inside the hole that if electrons reach the walls or hole-edges, stronger multiplication would occur. However it was unclear if electrons following the field lines during their drift reach this area of the hole.

Optical recording of avalanche-induced photons offers some advantages over electronic charge readout. It enables full decoupling of the detector from the readout system, with potential reduction of the readout noise. In addition, modern off-the-shelf CCD/CMOS cameras and image intensifiers offer adequate spatial resolutions for some applications, though at limited acquisition rates. These make optical readout an interesting tool for low-rate experiments; e.g. they are very useful in studies of rare events, of typical patterns, buried within high experimental background. For a review on optical imaging detectors see [12] and references therein.

Photons are created in gaseous detectors by direct excitation and de-excitation of the gas atoms and molecules [47]. In particular, photons are emitted during the avalanche process [48]. The emission yield (photons/avalanche electron) and the emission spectrum are a function of the gas, its pressure and the electric field; the latter is dictated by the detector geometry. Examples of gases with a high photon yield are mixtures of Ar with triethylamine (TEA) [49], some gases with Tetrakis dimethylamino ethylene (TMAE) [35], Ar or Ne with CF_4 [36,37], and N_2 with CO_2 [50]. CF_4 , used in this work, has some very convenient properties: it is a suitable quencher, absorbing secondary VUV photons while emitting photons copiously in the visible band – making possible the use of standard optics. For more information on the scintillation properties of CF_4 and its uses in gas detectors see [36,37,51,52].

Avalanche-induced photon readout can be used for various applications involving charged-particle tracking, single-photon localization in Cherenkov Ring Imaging [35], thermal neutron imaging [39,53,54] etc. Examples of optical recording of rare-event tracks in TPC detectors can be found in [55,56]. Lately, it has been proposed to optically record avalanches from Thick Gas Electron Multiplier (THGEM [20]) holes in liquid argon [57] and in xenon [58], with G-APD sensors.

Besides radiation-imaging applications, the precise localization of light emitted in the avalanche could be useful for studying basic electron transport and multiplication processes. It could provide useful information on the avalanche shape, size, diffusion, secondary effects etc. In this work, we investigated the potential of the optical readout method for studying basic avalanche processes in THGEM detectors.

Two independent experiments were performed. First, we irradiated THGEM detectors with different numbers of cascaded elements—using a non-collimated x-ray source; we were able

to measure the hole-multiplicity (number of activated holes per photon interaction) in different multiplier configurations. Second, we used a collimated x-ray source and measured the asymmetric development of electron avalanches within a hole, as function of the irradiation geometry. While we demonstrated the validity of the method in THGEM detectors, investigated by us for a variety of applications [20], it should be applicable to a large range of other electron multipliers.

4.2 Experimental Setup & Methodology

The experimental setup can be divided into three parts: the radiation source, the irradiated detector emitting the avalanche photons and the optical readout system recording these photons. Figure 8 shows the detector scheme (here with a double-THGEM assembly) and the optical apparatus. The radiation sources used in both experiments were significantly different; therefore we defer their description to section 4.2.3.

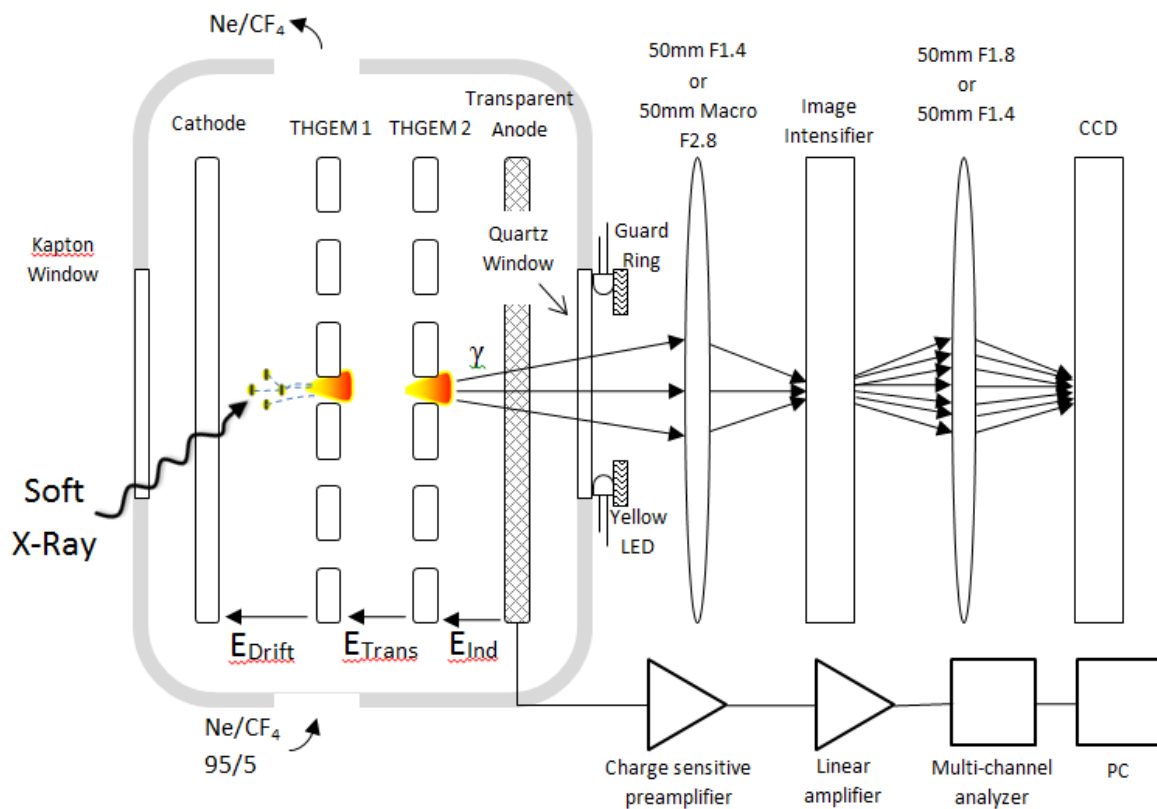


Figure 8: Experimental setup. The detector shown combines a cathode, a double- THGEM, and a wire-mesh anode. The light emitted by radiation-induced avalanches is recorded through a quartz window, by an image intensifier viewed by a lens, amplified and then focused by a second lens onto a CCD camera.

4.2.1 Detector Setup

The detector (single-, double- or triple-THGEM) was assembled in an aluminum chamber; it was continuously flushed with 1 atm of Ne/CF₄ (95/5), using an MKS 146 mass-flow control

system. The chamber had a 50 μ m thick Kapton x-ray window, and on the opposite end it had a 43mm diameter quartz window through which the emitted photons were collected by the optical setup. Yellow LEDs (with a guard ring of inner diameter 29mm) were placed outside the window. The parameters of the 30x30mm² THGEM electrodes employed in this work are summarized in Table 1.

Table 1: THGEM geometries investigated for avalanche asymmetry

THGEM #	Pitch (a) [mm]	Hole Diameter (d) [mm]	Thickness (t) [mm]	Rim size (h) [mm]
1	1	0.5	0.4	0.1
2	1.3	0.7	0.4	0.1
3	1.5	0.8	0.8	0.1
4	1.3	0.7	0.8	0.1

A cathode electrode (here, typically aluminized Mylar or a THGEM electrode) placed in front of the drift gap (Figure 8) supplied a potential to drift the electrons into the detector; a metallic mesh (of 82% optical transparency) following the induction gap collected the avalanche charge while allowing the emitted photons to pass through. The electrodes were biased with CAEN N471A power supplies through low pass filters. The avalanche charge was collected and read out through an Ortec 142 charge sensitive preamplifier. The signal was then amplified with an Ortec 570 linear amplifier and the spectrum and rates were measured with an Amptek 8000A multi-channel analyzer (MCA).

4.2.2 Optical setup

Avalanche photons were collected and imaged by an intensified CCD camera, in the optical setup shown schematically in Figure 8. Avalanche light traversing the chamber's quartz window was collected and focused with a lens (Nikon AF Nikkor 50 mm 1:1.4D or Sigma 50mm F2.8 EX DG Macro) onto a Proxitronic image intensifier, powered by a Topward dual-tracking DC power supply 6303D.

The intensifier, with an active photocathode diameter of 25mm, was type 2563MZ-V 100N dual-MCP, in a V-Stack assembly. The photocathode was type S20; the intensifier's P43 phosphor screen had a 1ms decay-time. The image intensifier was operated at 1640V (~90% of the maximal allowed amplification voltage).

The phosphor screen was then imaged onto a Finger Lakes Instrumentation CCD camera model MX0013307 with a 50mm lens (Canon FD 50 mm 1:1.8 or Nikon AF Nikkor 50 mm 1:1.4D) and recorded via USB. The images were acquired with a 50ms exposure time and were taken at a rate of ~3-5Hz. The detected x-ray rates of 4-30Hz were set to reduce

recorded-events overlap in a given frame (overlap < 10%). Due to the short exposure times the thermal CCD noise was insignificant, therefore there was no need to cool it. Examples of images obtained in different configurations can be seen in Figure 9.

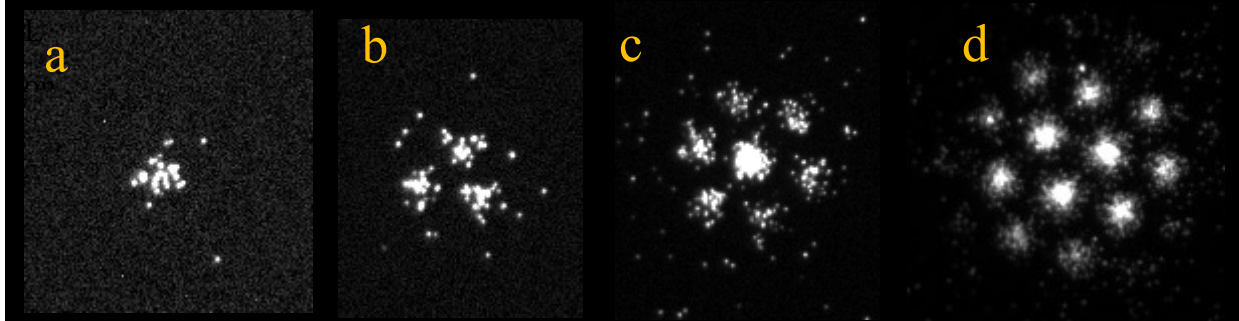


Figure 9: Examples of non-collimated 5.9keV x-ray induced single-event avalanches recorded in different detector configurations of the setup shown in Figure 8. a) Single THGEM with a reversed drift field of 0.3kV/cm and gain $\sim 10^4$; b) Single THGEM (E_{drift} 0.5kV/cm, gain $\sim 10^4$); c) Double THGEM with 8mm transfer gap (E_{drift} 0.5kV/cm, E_{trans} 0.5kV/cm, gain $\sim 5 \times 10^5$); d) Triple THGEM with 8mm and 10mm transfer gaps (E_{drift} 0.5kV/cm, E_{trans} 0.5kV/cm, gain $\sim 10^7$). The images are unprocessed, but the contrast has been adjusted to improve visibility. THGEM type 1, Table 1.

In order to determine the geometrical position of the detector's holes it was illuminated from outside the chamber with yellow LEDs.

The photon-yield reaching the CCD camera was estimated in the following way: avalanche photons were transmitted through the anode mesh, of 82% optical transparency; they were collected by the first lens (imaging the detector onto the image intensifier) at a solid angle of $\sim 7\%$, with the lens transmission of $\sim 90\%$; the S20 photocathode had $\sim 6.5\%$ quantum efficiency at the main Ne line (586nm); the double MCP had a gain of $\sim 10^4$; the phosphor screen released ~ 185 photons/e at a wavelength of ~ 545 nm; it was viewed by the second lens (imaging the phosphor screen onto the CCD) with a solid angle of $\sim 1.5\%$ with a transmission of $\sim 90\%$; the CCD had a quantum efficiency of $\sim 65\%$ at 545nm.

Following Tokanai et al. [38] we roughly estimated the avalanche-photon yield (above 400nm) for our Ne/5%CF₄ mixture, to be ~ 0.06 photons/e. There is no data in the literature discussing the photon yield from this gas mixture, however similar work with GEMs in Ar/CF₄ [37] indicated a minimal difference between 5% and 10% CF₄ (0.57ph/e- and 0.54ph/e- respectively), though at gains <100. Tokanai et al. measured a $\sim 90\%$ drop in the photon yield between Ar/10%CF₄ and Ne/10%CF₄ for gains of $\sim 10^4$ in a capillary plate (CP) gaseous detector [38].

Based on the above, 8keV x-rays (depositing ~ 230 electrons per event in Ne/5%CF₄), at detector gain of 10^4 , will release on the average ~ 440 photoelectrons from the photocathode

of the image intensifier, resulting in photon yields of $\sim 7 \times 10^6$ electrons/x-ray created in the CCD.

The images recorded by the CCD contained two types of noise: CCD thermal pixel noise and the noise from the image intensifier itself. Figure 9 shows that avalanches, being formed of densely distributed spots, are clearly distinguishable whereas the random noise is sparse. The image processing was done using built-in functions of the Mathworks Matlab® R2012a Image Processing Toolbox [59]. The CCD noise was eliminated by subtracting an image taken with the shutter closed, setting a threshold on the intensity at the mean plus twice the standard deviation (leaving a binary black and white image), and applying a 3x3 pixel median filter.

The image intensifier noise was eliminated by applying a morphological closing filter—using a disc-shaped structuring element with a radius set to be roughly half the radius of a hole—then discarding all information outside the holes and applying an area criterion: if the multiplicity was >1 , a spot was kept only if its area was larger than 50% of the area of a hole; if the multiplicity was 1, a spot was kept only if its area was larger than 80% of the area of a hole. Only events that were far from the edges of the frame were considered, to avoid underestimating the multiplicity. Figure 10 shows an example of an image before and after processing.

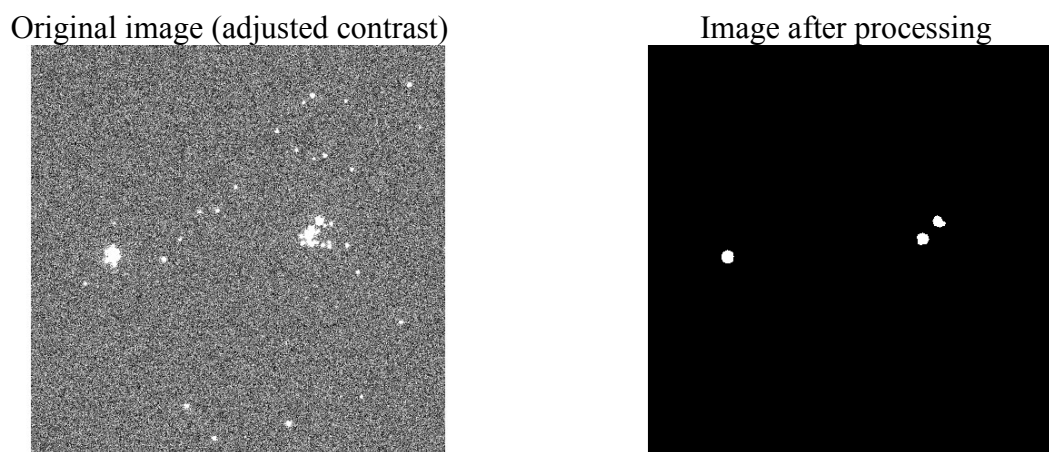


Figure 10: Example of the image before (left) and after (right) processing. Three holes were identified: one event had a hole-multiplicity of two and the other had a multiplicity of one.

4.2.3 Description of the assays

The two assays performed were different conceptually. In the first, a single-THGEM type was used, and several THGEMs were cascaded to provide small and large hole-multiplicities. In the second, a collimated source was scanned across the hole of different THGEM types

(different hole-sizes and thicknesses) and the avalanche asymmetry within the hole was studied.

4.2.3.1 Hole multiplicity for different detector configurations

The detector was irradiated with 5.9 keV x-rays from a non-collimated ^{55}Fe source. The detector consisted of a THGEM with 1.2mm diameter holes as a drift electrode to bias the drift gap, one or more THGEMs separated by transfer gaps, and a metallic mesh to bias the induction gap and collect the charge. The THGEMs used to multiply the electrons were Type 1, Table 1. The configurations and fields are given in Table 2. Several thousand CCD frames were captured and analyzed in each configuration.

Table 2: The configurations used to study the hole-multiplicity with a THGEM (type 1, Table 1)

Configuration	Number of cascaded THGEMs	THGEM Voltages [V]	Gain [AU]	Drift gap [mm]	Drift field [kV/cm]	Transfer gaps [mm]	Transfer fields [kV/cm]	Induction gap [mm]	Induction field [kV/cm]
a	1	830	$\sim 10^4$	10	Inverted 0.3	-----	-----	5	0.5
b	1	830	$\sim 10^4$	10	0.5	-----	-----	5	0.5
c	2	650,750	$\sim 5 \times 10^5$	10	0.5	8	0.5	5	0.5
d	3	700,650,600	$\sim 10^7$	10	0.5	10,8	0.5, 0.5	5	0.5
e	3	450,600,700	$\sim 10^6$	10	0.5	2,2	0.5, 0.5	5	0.5

4.2.3.2 Scan across hole with collimated x-ray beam

The detector was irradiated with a collimated 330 μm (FWHM) broad 8keV x-ray beam (Figure 11). It was precisely displaced allowing for beam positioning at different locations relative to a hole center (in $\sim 140\mu\text{m}$ steps) as is illustrated in Figure 12.

X-Ray beam collimation and localization

The x-ray beam was prepared by using an Oxford Instruments Cu target x-ray tube. The x-ray tube had a focal spot size of 80x120 microns; its intensity was attenuated with ~ 30 micron thick copper foils; the beam was collimated with a 0.5mm circular aperture placed $\sim 210\text{mm}$ from the focal point and a 120 micron slit placed $\sim 90\text{mm}$ from the 0.5mm collimator. The detector was placed $\sim 100\text{mm}$ from the slit (Figure 11).

The beam profile was measured by placing the x-ray tube in front of the slit and behind them an Amptek XR-100CR silicon x-ray detector with a 200 μm slit attached to it; the silicon detector and slit were displaced horizontally and vertically (with the slit rotated). The beam profile was determined from the yield of the K_{α} line of Cu (8keV), thus avoiding any influence from incoherent scattering. The beam was measured to be 380 μm by 760 μm

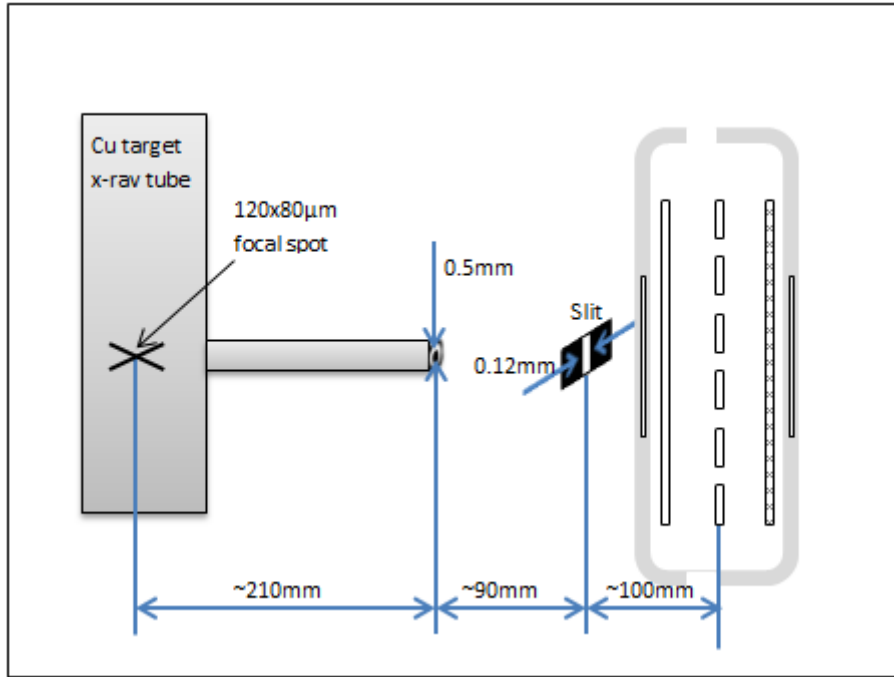


Figure 11: Experimental setup for scanning across a THGEM hole with a collimated x-ray beam (dimensions not to scale).

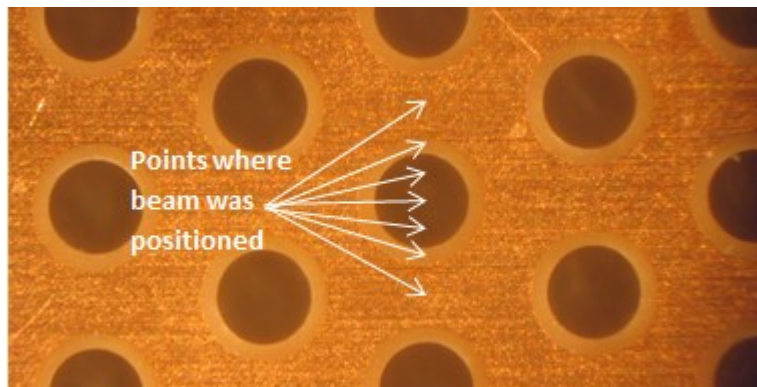


Figure 12: Irradiation locations throughout x-ray beam scanning across a THGEM-hole.

(FWHM). Correcting for the slit width of $200\mu\text{m}$, the estimated beam dimensions were $330\mu\text{m}$ by $730\mu\text{m}$ (FWHM).

Measurement sequence

The x-ray beam's position was determined by placing a ZnS(Ag) screen in the focal plane and fitting the spot to a Gaussian. Only the detector was displaced in the experiments, therefore the pixel representing the position of the beam remained fixed and the detector was moved relative to this pixel manually.

For each image, the center of gravity of the light emitted from the scanned hole —after subtracting the mean intensity—was calculated. The centers of gravity were aggregated into a histogram—one for the x coordinate and one for the y coordinate—and fit to a Gaussian; its

mean being the offset of the centroid from the center of the hole. An example where the beam was positioned in-between holes is given in Figure 13a and Figure 13b; in both holes the light emission is asymmetric, shifted towards the beam's position. In order to verify that the algorithm was producing reasonable results, a histogram showing the number of times each hole participated in an event was plotted. Figure 13c shows that the holes closest to the estimated beam position are most active, with the activity decaying with distance.

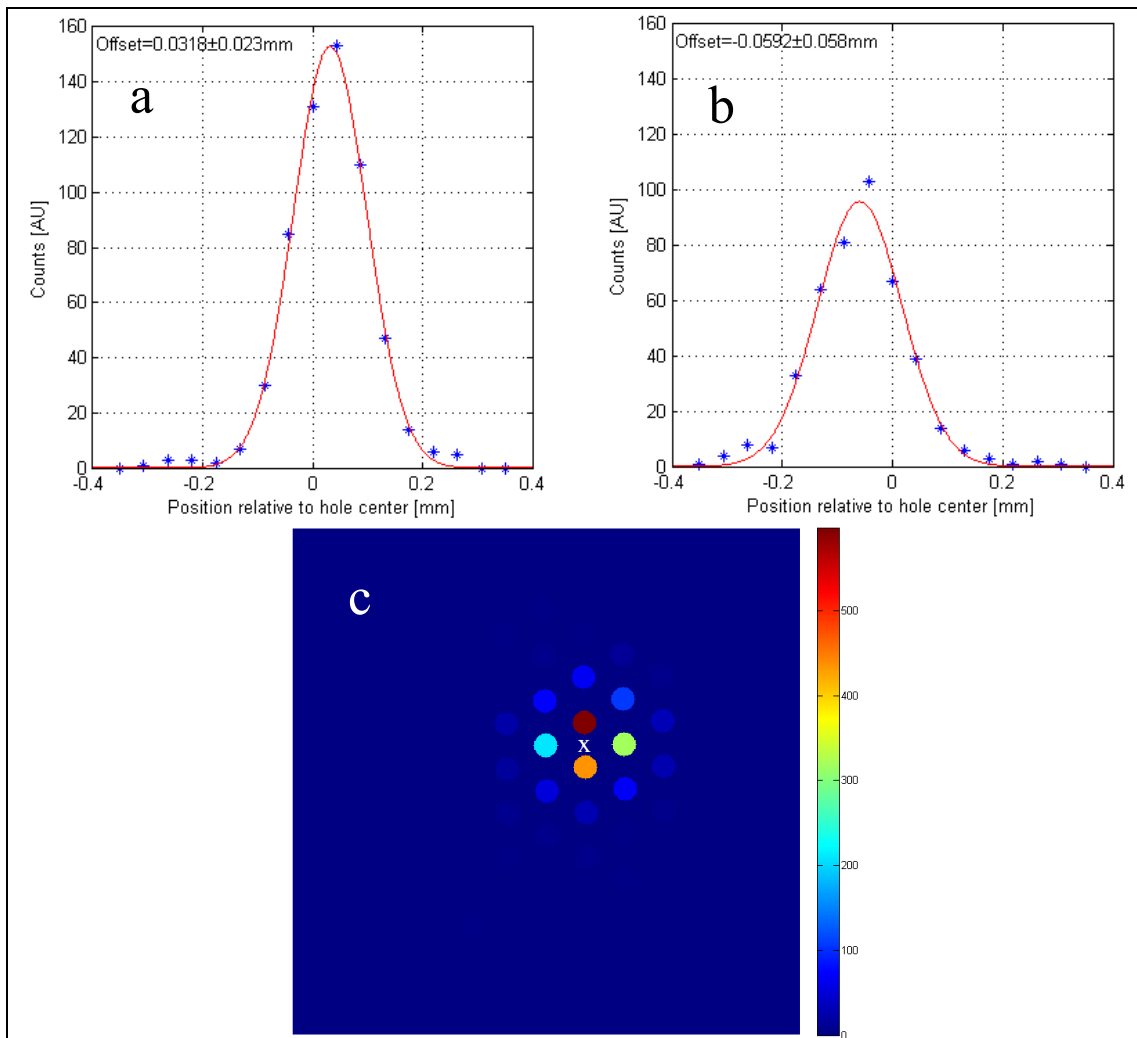


Figure 13: Scanning across a THGEM hole (see Figure 12). Shown are the analysis results with the x-ray beam positioned in between two holes. a and b) histograms of the centroid of the light distribution in the vertical direction in holes located above and below the beam. The distribution in both holes is offset in the direction of the beam. c) Color coded image, with a color corresponding to the number of times a hole participated in an event (the cross being the predicted beam position deduced from the image on the phosphor screen). Detector gain 10^4 .

Geometries studied

The study was conducted on a detector with an aluminized Mylar drift electrode supplying a 0.5kV/cm drift field over a 5mm gap, a single-THGEM multiplier and an anode mesh; a 0.5kV/cm induction field was set over the 5mm induction gap. Several THGEM electrodes were investigated, with different parameters depicted in Table 1.

A second assay was performed by using THGEM#1 (Table 1), biased for an effective gain of $\sim 10^4$, keeping the induction field at 0.5kV/cm and varying the drift field from 0.2 to 1.5kV/cm. The configurations tested are given in Table 3.

Table 3: The drift field configurations of a single-THGEM (#1 in Table 1) detector scanned across with a collimated x-ray beam (Figure 11).

Configuration	Drift gap [mm]	Drift field [kV/cm]	Induction gap [mm]	Induction field [kV/cm]
f	5	0.2	5	0.5
g	5	0.5	5	0.5
h	5	1.0	5	0.5
i	5	1.5	5	0.5

4.2.3.3 High statistics runs and simulations

In order to assess the distribution of events when irradiating at different locations, two high-statistics runs were conducted with THGEM type 1 in configuration g, collecting 15,000 events with the beam positioned at the center of a hole, and 20,000 events with the beam positioned in between adjacent holes. This was compared to the following simulation: a THGEM type 1 in configuration g was simulated in ANSYS [60] with 800V across the THGEM. Using Garfield [28], 8keV electrons were released and let to ionize the medium. We define the THGEM plane to be x,y and z to be the axis connecting the THGEM with the anode and cathode. Every electron created along the ionization path was allowed to drift through the THGEM and the position (x,y) was recorded where it crossed the bottom edge of the THGEM—~230 electrons were followed for each 8keV electron released. No electron multiplication was allowed. The 8keV electrons were released uniformly along the z axis in the drift gap. Four assays were performed: releasing the electrons above the center of a hole and in between adjacent holes with the x,y distribution having zero width (delta function input); and repeating with the x,y distribution being Gaussian with FWHM of 330 μ m and 730 μ m in the vertical and horizontal directions, mimicking the x-ray beam size described above. For each assay 5×10^4 8keV electrons were released. The center of gravity of each event was calculated as the center of gravity of the x,y coordinates of the electrons exiting the THGEM.

4.3 Results

4.3.1 Hole multiplicity for different detector configurations

Figure 14 shows the measured multiplicity distribution for the configurations given in Table 2. The figure indicates that events from the uncollimated 5.9keV X-rays were found to span

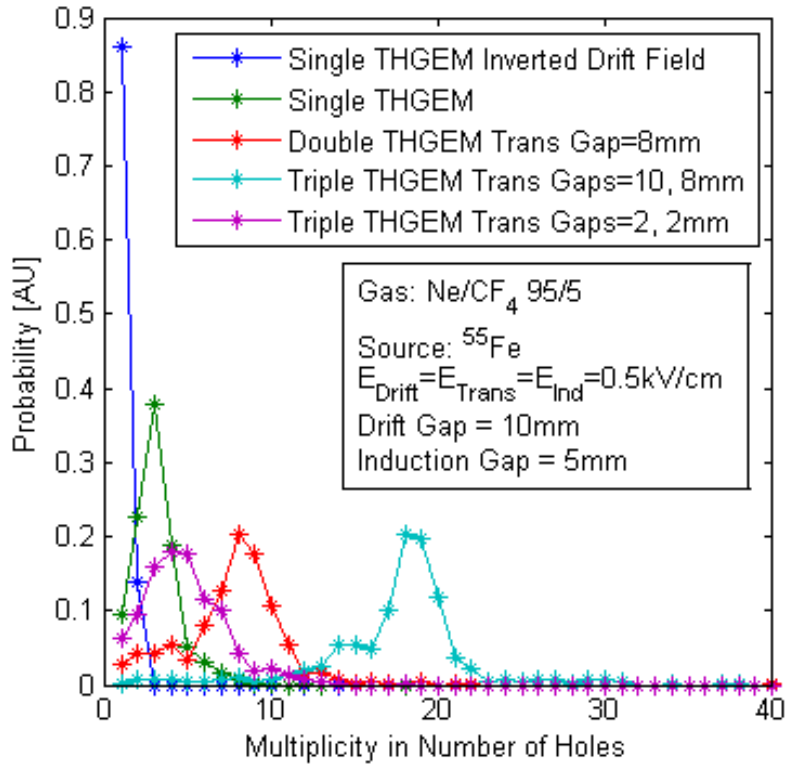


Figure 14: Multiplicity distribution for different configurations (Table 2) of the THGEM detector (type #1, Table 1).

1-20 holes depending on the detector configuration. The inverted drift field (resulting in conversion close-to and within holes) resulted in a multiplicity of 1 in 86% of the events. While the gain was not kept fixed between the assays, we can see that qualitatively the multiplicity is strongly affected by large transfer gaps; reducing the transfer gap in the configuration e (Table 2) reduced the multiplicity significantly.

4.3.2 Scan across hole with a collimated x-ray beam

Figure 15 shows the results of measurements of the avalanche displacement as function of position of irradiation for the geometries in Table 1. Shifting the relative position of the x-ray beam to the hole center shifted the light-emission distribution from the hole (Figure 15a). No shift was apparent in the direction perpendicular to the scan direction (Figure 15b). Changing the hole geometry and thickness as well as changing the drift field had a minor effect on the displacement of the avalanche (Figure 16). Figure 16 depicts the avalanche displacement as a function of the drift field measured with a detector (type 1 Table 1) in the configurations described in Table 3. It shows that changing the drift field at constant gain has small influence on the distribution of light inside the hole. A seven-fold increase in the drift field (at the same gain) caused a maximal shift of 0.09mm as opposed to 0.065mm.

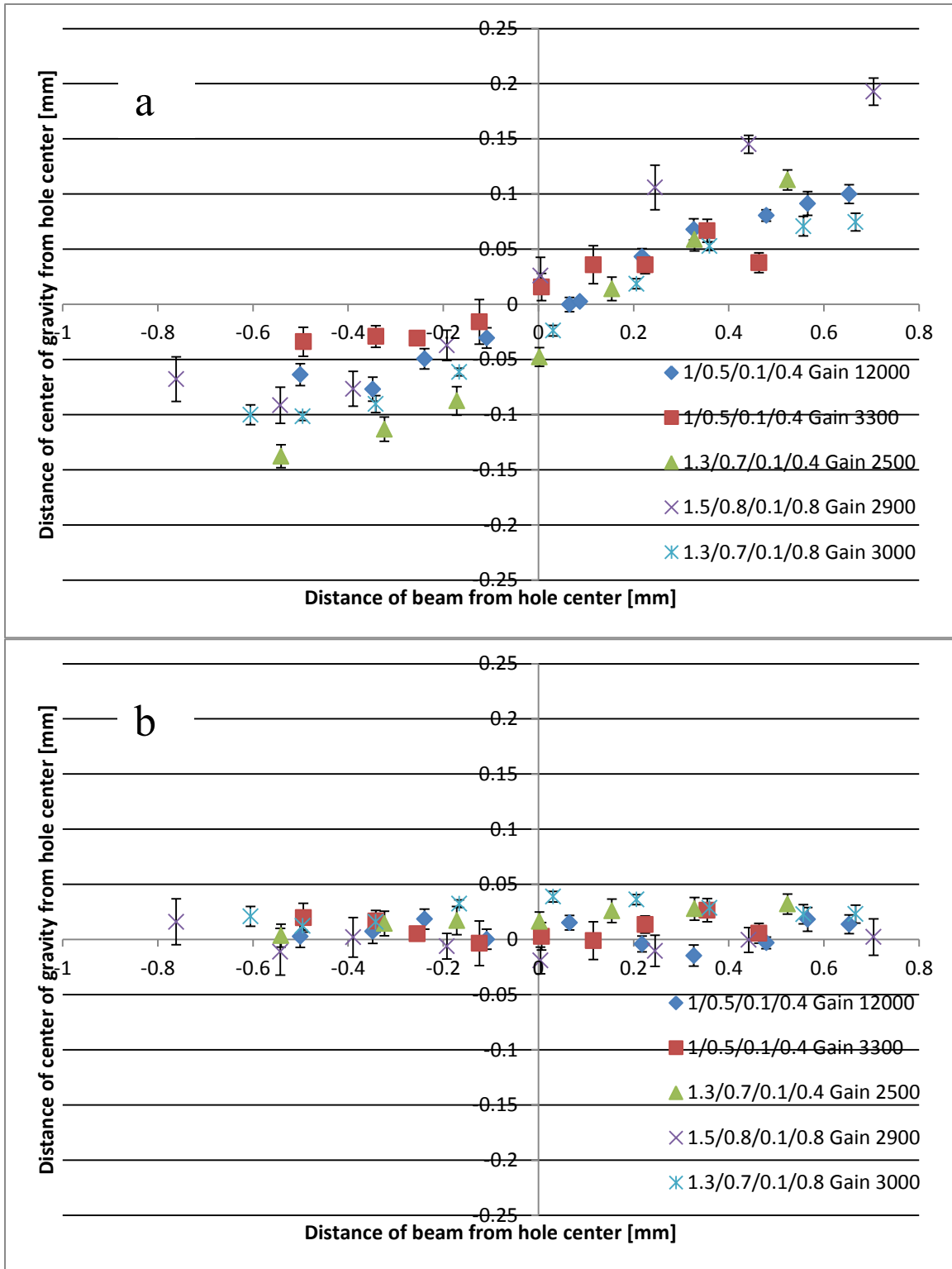


Figure 15: Results of scanning with a collimated Cu x-ray beam across a hole. a) In the direction of the scan. The centroid is correlated with the relative position of the beam. The effect is more pronounced in the larger-hole THGEMs. b) In the perpendicular direction of the scan no correlation is apparent. The slight bump towards the center is due to a geometric effect stemming from alight misalignment of the beam. Error bars are the 95% confidence level of the Gaussian fit. The gains and THGEM geometries (a,d,h,t) are provided in the figure; gas Ne/5%CF₄.

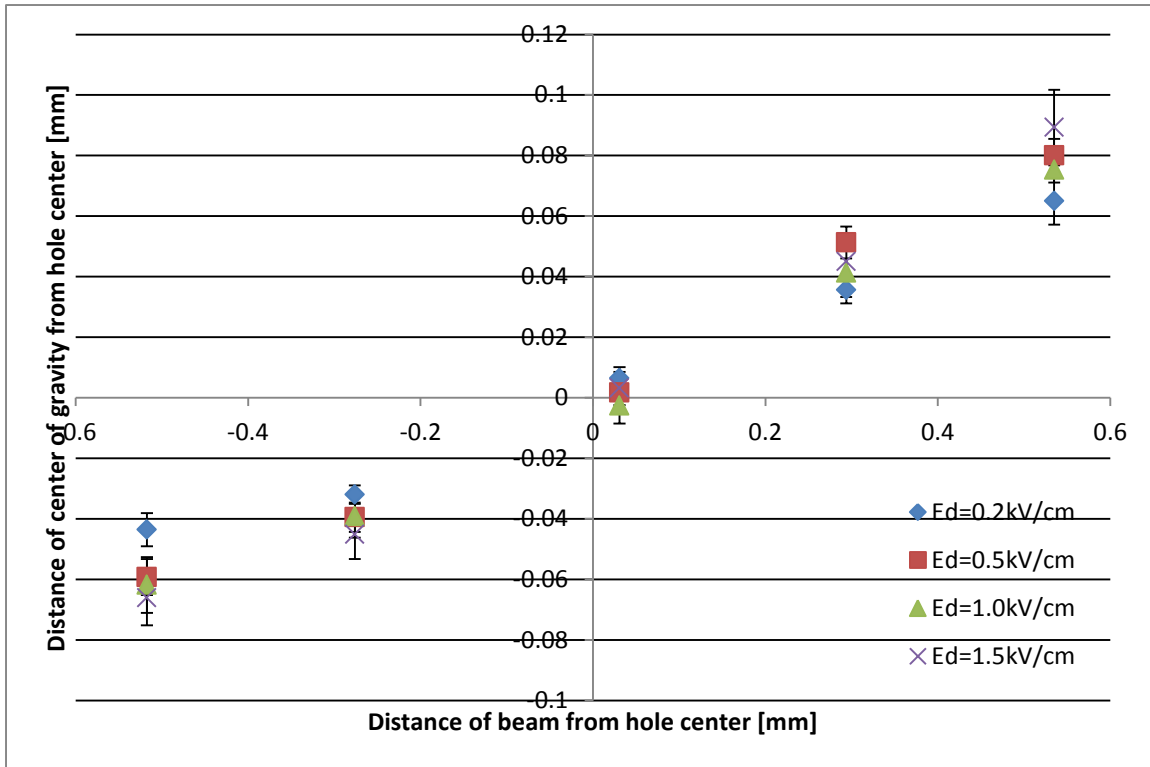


Figure 16: Drift field scan for THGEM (type #1, Table 1) operated at a gain of 10^4 in field configurations according to Table 3. Drift fields (E_d) are shown on the figure. Error bars are the 95% confidence level of the Gaussian fit.

4.3.3 High statistics runs and simulations

Figure 17 depicts the results of the high statistics runs ($>10^4$ events), taken at 10^4 gain at the center of a hole and in between holes described in section 4.2.3.3. It shows how the center-of-gravity of the light (experiment and simulation) is distributed—for irradiation at the center of the hole and in between holes respectively. Figure 17a shows the distribution of the experimental center-of-gravity for irradiation at the center of the hole. Most event's center-of-gravity fell at the center of the hole. However many events divided between two adjacent holes—causing the center-of-gravity to fall in between them; this is the reason for the star shape that is visible in the figure. Figure 17b shows when the detector was irradiated in between holes, the center-of-gravity fell primarily in between them (the strong line connecting the holes). Table 4 compares the distributions of the experiments and the simulations. Experimentally 95% percent of the events were found to be within 1.4mm of the point of irradiation, both when the beam was at the center of a hole and when it was in-between holes.

Table 4: Radius containing 33, 66 and 95 percent of the center-of-gravity of the events (experiment and simulation) when irradiating the center of a hole and in-between holes for a THGEM (type 1, configuration g) and a gain of 10^4 . Images are given in Figure 17.

		Radius containing 33% of events [mm]	Radius containing 66% of events [mm]	Radius containing 95% of events [mm]
Experiment	Irradiation at center of hole	0.45	0.67	1.4
	Irradiation in between holes	0.43	0.73	1.4
Simulation Delta function	Irradiation at center of hole	0.69	0.96	1.32
	Irradiation in between holes	0.71	1.04	1.33
Simulation Gaussian beam	Irradiation at center of hole	0.8	1.2	1.9
	Irradiation in between holes	0.79	1.2	1.88

4.4 Discussion on the optical recording of avalanches

We found that it was possible to count the number of holes involved in single photoionization events using optical readout. The parameters that play a role in the hole-multiplicity of the detector are the size of the initial electron track, the point of interaction, the length and fields of the drift and transfer gaps, and the diffusion properties of the gas mixture used. For example for ^{55}Fe used in this work, the 5.9 keV photoelectron induced on the average 164 electron-ion pairs in $\text{Ne}/5\%\text{CF}_4$ along a track length² of $\sim 900\mu\text{m}$. The initial electron cloud diffuses and subsequently reaches several holes. In $\text{Ne}/5\%\text{CF}_4$ the diffusion coefficient at 0.5kV/cm is $\sim 250\mu\text{m}/\sqrt{\text{cm}}$, indicating a substantial spread between stages. The event spread grows with the number of multiplication stages and the width of the gaps between them—due to diffusion and to additional photon-induced secondary effects. In this work, single events extended over diameters up to ~ 6 mm, for a triple-THGEM structure with 8-10mm drift and transfer gaps.

The inverted drift field prevented primary electrons created in the drift gap from reaching the multiplication stage. Therefore, only photons that interacted within the THGEM hole were multiplied—illuminating single holes. Figure 14 shows that the multiplicity of this configuration was in fact one, in agreement with our expectation. Increasing the number of stages caused higher multiplicity due to diffusion and the discretization of the THGEMs holes. A somewhat surprising result was that the multiplicity of a triple THGEM with small transfer gaps has a multiplicity that is close to that of the single staged detector. This is

² This was simulated with HEED [27] by releasing 5.9keV electrons in $\text{Ne}/5\%\text{CF}_4$ and measuring the range of the track created. The range obtained from the approximation $R_p = 0.71E^{1.72}$ (E in MeV, R_p in g cm^{-2}) [26] for pure neon is 1.24mm.

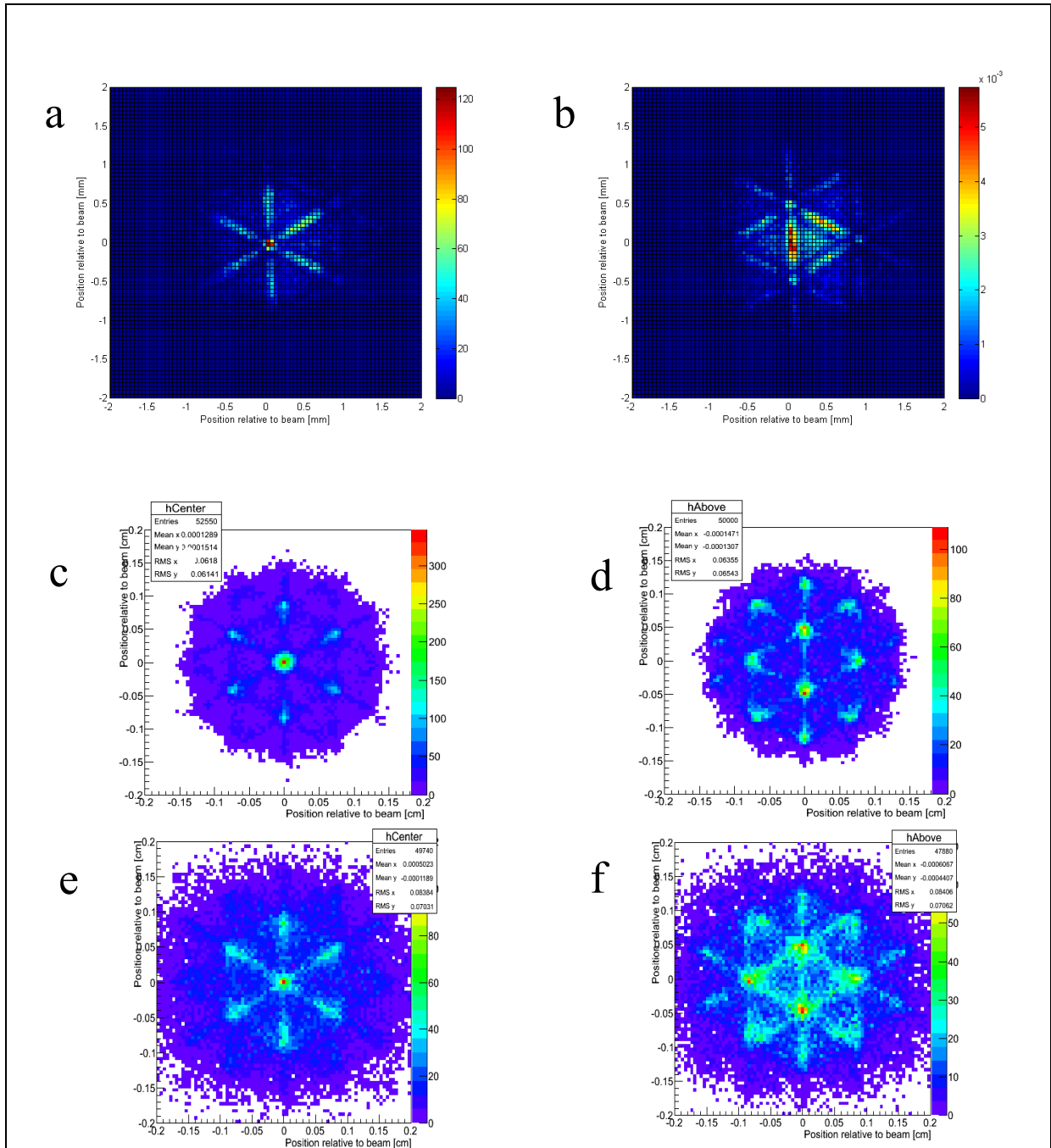


Figure 17: Reconstruction of the points of interaction—from the center-of-gravity—when irradiating the center of a hole and in between holes for a THGEM type 1 configuration g. a) and b) are experimental results of $\sim 10,000$ events at 10^4 gain; c) and e) are center-of-gravity for simulating (section 4.2.3.3) 8keV electrons above the center of a hole, for a delta function distribution and a Gaussian distribution of width $330 \times 730 \mu\text{m}$ FWHM respectively; d) and f) the same but for irradiation between neighboring holes. See text for explanations of the figures.

encouraging because multiple staged devices have many advantages, primarily in their stability during high gain operation [10].

The results of the present study should however be treated qualitatively. A broader systematic study—measuring the dependence on the gain, the gap size, the division of voltage between stages—may extend the results shown in Figure 14; such a systematic study was beyond the

scope of this work. However, our results suggest that optical readout would be an appropriate tool to conduct such a study.

The objective of this demonstration was to explore what information is contained in the distribution of light within a THGEM hole. Figure 15 shows that there is a clear correlation between the position of irradiation and the distribution of light within a hole. In all of the THGEMs measured, the center of gravity of the light inside the hole was only mildly displaced from the center (<50% of the radius of a hole). The electric field is strongest at the edge of the hole [13], indicating increased multiplication. However, the electric field lines drifting the electrons indicate that electrons do not reach the holes edge. A priori it is unclear which process is dominant. We conclude from the results (Figure 15) that although the electric field is higher near the edges of the hole, the displacement of the avalanche from the hole's center is not a major effect; indicating that the avalanche develops primarily away from the edge. We draw the same conclusion from the manipulation of the drift field (Figure 16): although the drift field influenced the displacement of the avalanche, the effect is rather weak. Our conclusion is that in THGEM detectors, the avalanche develops primarily away from the edge of the hole.

Collecting high statistics by irradiating the center of a hole, and in-between adjacent holes, was instructional in two ways. First, visualizing the two-dimensional distribution of the center of gravity displays many of the important features of the detector. For example, in Figure 17a, the strong lines connecting adjacent holes indicate that most events divide between two holes. These features require deeper study, as they may depend on the type of algorithms used to identify avalanches; specifically, if the low-charge events are cut, this has a large impact on multiplicity estimation.

More importantly, 95% of the events occurred within 1.4mm of the estimated beam position. This agrees with the photoelectron range in Ne/5%CF₄—which simulation shows to be 1.55mm (the projection onto the x-y plane is 1.26mm)—and roughly to what was produced by simulating the drift of electrons. We also see that the size of the reconstructed beam profile is independent of the position of irradiation in both cases. This result is reasonable in light of the fact that the photoelectron range is of the order of the distance between holes.

Making the beam in the simulations the same shape as what was used in the experiment (Figure 17d and Figure 17f) resulted in better agreement with experiment, showing increased reconstruction along the lines connecting holes. However in the experimental results the

adjacent holes are not highlighted, while in the simulation they are. The differences between simulation and experiment may be due to the fact that electrons were drifted without multiplication—a process that is computationally prohibitively time consuming.

We have shown here that optical recording of detector avalanches could be a powerful tool for studying the parameters and behavior of gaseous detectors. It can assist in optimizing detector geometry and configuration, gas mixture and operation gain. Another effect of interest is photon-feedback—which would manifest as multiple satellite events in the same frame. The high granularity of the CCD readout provides the opportunity to probe the physics processes inside holes.

5 Investigations of Resistive-Plate WELL (RPWELL)

5.1 Introduction

One can identify two major trends in the world of gaseous radiation detectors with regards to discharges: elimination and mitigation. The Resistive Plate Chamber (RPC), developed in 1981 [61], adopts the former approach. RPCs are constructed with highly resistive materials ($\rho=10^7\text{-}10^{12}\ \Omega\text{cm}$) such as Bakelite, glass or antistatic plastics set in a parallel plate geometry. Figure 18 shows an example of an RPC. The plates are separated by a few mm (the ATLAS RPC Level-1 muon trigger uses 2mm gaps [62]) and are coated on the outside with graphite paint—this is used to confine the signal for temporal and spatial positioning and for biasing the plates with high voltage. Outside the graphite paint and behind a thin insulating layer, aluminum strips (termed X and Y readout strips in the Figure 18) are placed to pick up and read out the signal. A typical RPC gas, from the BABAR experiment is argon (48%), $\text{C}_2\text{H}_2\text{F}_4$ (48%), isobutane (4%) [63].

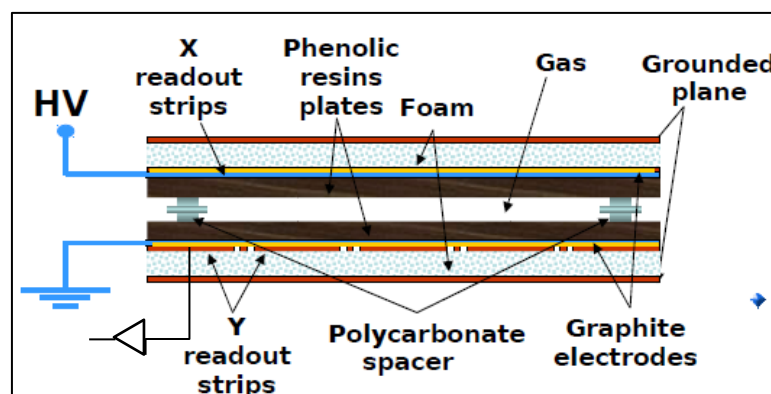


Figure 18: Example of RPC.

The signal induced on the strips is given by the Ramo theorem [64]

$$i(t) = q\vec{E}_w \cdot \vec{v} \quad (5)$$

where $i(t)$ is the induced current, \vec{v} is the velocity of the charged particle and \vec{E}_w is the *weighting* field at the position of the charged particle. The weighting field is calculated by setting a unit potential on the electrode on which the current is induced and zero potential on the rest of the electrode in the system.

The high resistivity of the RPC plates limits discharges geometrically to very small areas ($\sim 10\text{mm}^2$) [65]; the high resistance inhibits the motion of charges on the plates, causing the time constant of the current to be much larger ($\sim 10^{-2}\text{s}$ -1s, depending on the resistivity of the plates) than the time constant necessary to maintain the discharge ($\sim 10\text{ns}$) [65]; therefore after a small flow of charge between the plates, the potential difference collapses extinguishing the discharge. Because the currents are small, the power supply can supply them while maintaining the voltage; therefore voltage drops are prevented. Initially very high voltages were applied to the plates, and very large signals were recorded without the need of further electronic amplification. This was later learned to be a “streamer mode” of operation—characterized by a discontinuous jump in the pulse height (Figure 19). This mode has the advantage of producing high signals, however these intense signals deposit large charge ($\sim 500\text{pC}$) in a region of $\sim 1\text{cm}^2$ [66]. The high resistivity of the electrodes required several tens of milliseconds to clear the deposited charge, limiting this mode of operation to a rate of $\sim 10^2\text{Hz/cm}^2$. Modern operation of RPCs is in the smaller-gain proportional mode (improving rate capabilities), requiring some electronic amplification, but reducing the amount of charge that needs to be evacuated. The transition to “streamer mode” has been extensively studied [67]: as the high voltage is increased the proportion of streamers increases (Figure 19). This discontinuity in signal height, and the coexistence of the smaller proportional events alongside the intense “streamer” events is typical of streamer tubes [68], and served as evidence that the high intensity signals were in fact “streamer” modes [66].

The high resistivity comes at the cost of rate capability and charge diffusion. RPCs are low-to-medium rate detectors, with high efficiency limited to rates on the order of kHz/cm^2 . Research is being actively pursued to find materials with bulk resistivity between 10^5 - $10^7\Omega\text{cm}$ [69]. Resistive ceramic (10^7 - $10^{12}\Omega\text{cm}$) RPCs have been shown to be fully efficient (Figure 20) up to $\sim 10^5\text{Hz/cm}^2$ [70] [71].

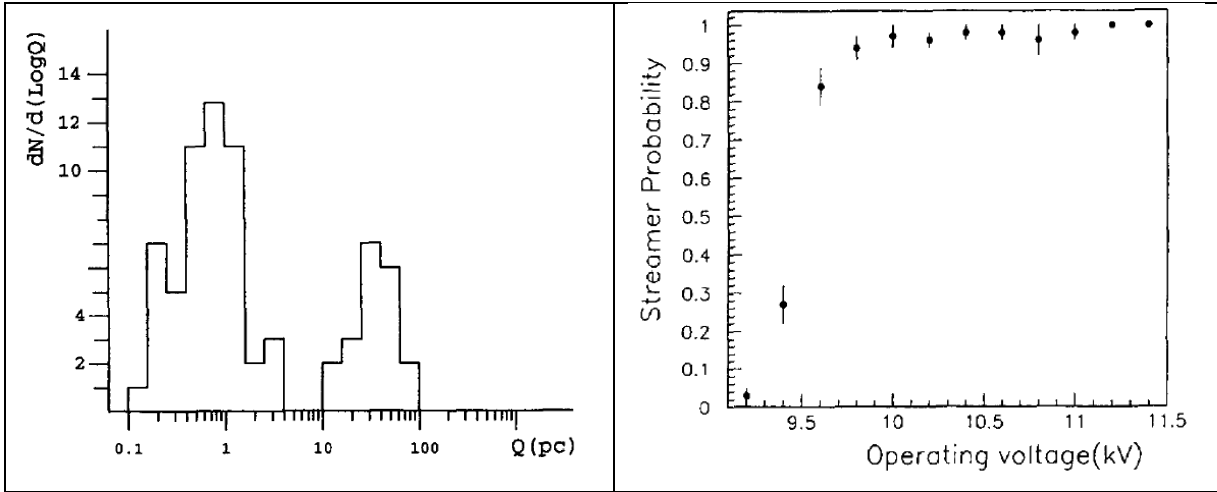


Figure 19: Pulse-height spectrum at 9.4kV, showing two groups of proportional- and higher-gain streamer-pulses (left) and streamer probability as a function of operating voltage for a 2mm gap RPC with Ar/n-C₄H₁₀/CF₃ 60/37/3. From [67].

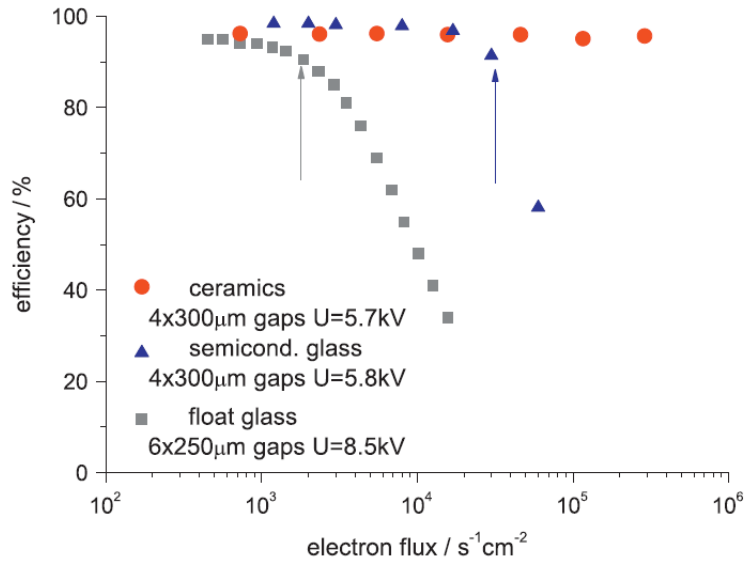


Figure 20: Efficiency of RPCs with different electrode materials (ceramics, semi-conductive- and float-glass) in dependence on the incident electron-beam flux. Taken from [70].

Although the rate dependence of the gain is well known in the RPC community, few attempts have been made to model the behavior. The key parameter that governs the RPCs rate response is given by time constant [65]

$$\tau = \rho\epsilon \quad (6)$$

where τ is the time constant, ρ is the bulk resistivity and ϵ is the permittivity of the material. Typical values are $\rho \sim 10^{12} \Omega cm$ and $\epsilon \sim 4\epsilon_0$, where ϵ_0 is the vacuum permittivity. These yield a time constant $\tau \sim 0.4s$. Abbrescia has suggested a model called the “single-cell model” in which the RPC is modeled as collection of capacitors [72]. Due to the simple planar geometry, the analytical relations between the charge on the plates and the voltage are easily found. In the single-cell model it is assumed that only a limited region is affected by

the avalanche: the incoming charge of the avalanche discharges the capacitor by an amount qG , where q is the primary charge and G is the gain. This causes a drop in voltage across the gap, and the next incoming particle will see a lower field and will undergo lower multiplication. The field is restored by the time constant of the resistive plates. Numerical solutions of this model show agreement with experimental rate dependence. Lippmann et al. has suggested a more complicated model [73], using the quasi-static approximation of Maxwell's equations. Solving for the field of a single particle, they were able to show field drops of $\sim 8\%$ at $6\text{Hz}/\text{mm}^2$ in a 3mm gapped RPC with 3kV. This should cause a large drop in gain, although they did not compare with experimental gain vs. rate data. Both approaches take advantage of the simple analytical solution for the field in an RPC (essentially a parallel plate capacitor).

The MPGD community has adopted solutions for spark mitigation: using resistive materials—on the order of $\sim 1\text{-}20\text{M}\Omega/\text{square}$ —to cover plain electrodes as well as segmented ones for charge readout with pads or strips. The spark probability remains the same, yet each spark's intensity is reduced, because the amount of charge that can flow is limited before the electric field collapses. A most successful example is that of the resistive MICROMEGAS [8] which will be integrated into the ATLAS muon tracking system. Before the modification to resistive readout, MICROMEGAS used a micro-mesh to generate a strong parallel-plate like field inducing an avalanche directly onto the readout strips. To protect against sparks, the detector has been improved and the avalanche is collected on $\sim 0.5\text{-}100\text{M}\Omega/\text{cm}$ strips separated by an insulator from copper readout strips (Figure 21). This detector has been shown to be undamaged by sparks [74]. However, a drop in gain as a function of rate has been observed, with drops of up to 25% for rates on the order of $10^7\text{Hz}/\text{cm}^2$. Other geometries with resistive layers have been tried with varying success: the Resistive GEM and THGEM (RETGEM) [75] and the resistive Micro Pixel Chamber (uPic) [76].

The Weizmann group has approached the problem in a similar fashion, suggesting the Segmented Resistive WELL (SRWELL) detector [23] [9]. The SRWELL (Figure 22) was an evolution of the THick-WELL (THWELL): a single-faced THGEM coupled directly to a copper anode that was proposed primarily to meet the thickness requirements of the Digital Hadronic Calorimeter proposed for the International Linear Collider [22]. In this configuration sparks on the detector propagate directly to the anode—potentially damaging

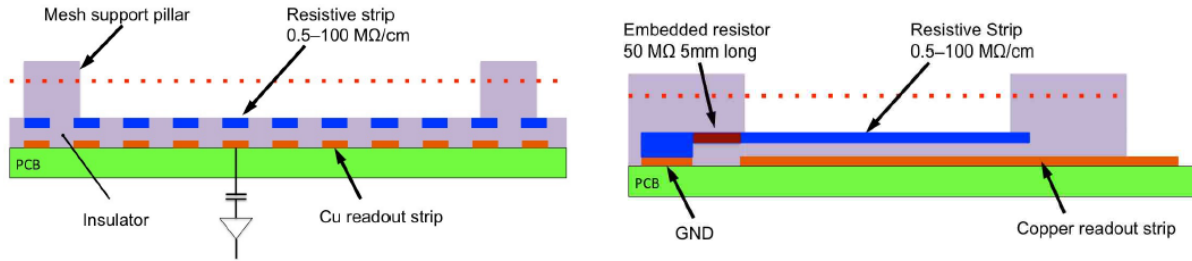


Figure 21: Schematic view (not to scale) of the resistive MICROMEAS concept. View along the strips (left) and side view orthogonal to the strip direction (right). From [8].

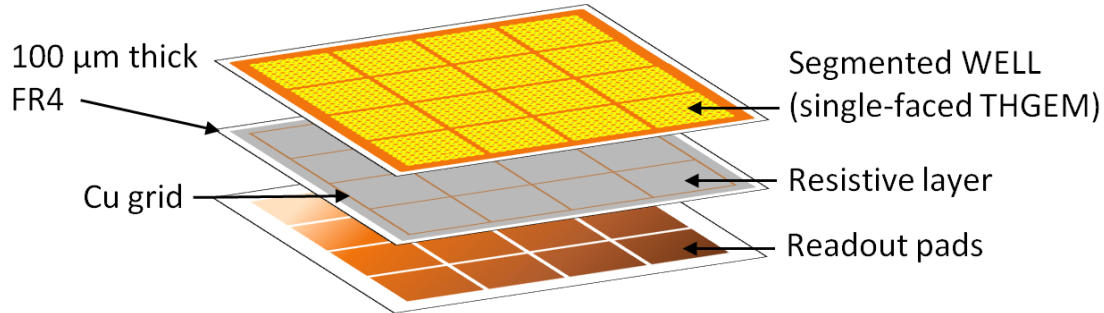


Figure 22: Schematic description of Segmented Resistive Well THGEM (SRWELL) coupled to a readout pad array. From [24].

the electronics. Therefore a 0.1mm layer of FR4 was covered with a resistive layer of graphite and epoxy—resistivity of $100\text{k}\Omega/\text{sq}$ – $20\text{M}\Omega/\text{sq}$ —and placed between the copper anode and the THGEM (RWELL). The induced charge on the copper anode was then read out. This proved to successfully reduce the intensity of sparks by roughly one order of magnitude. However, the charge on the resistive layer spread along the whole layer due to diffusion and caused strong cross-talk between neighboring pads of the readout. Adding a copper grid, to capture the charge, solved this problem and was successfully tested at a recent beam test in November 2012. I have participated in this R&D and took part in the beam tests at CERN and in the data analysis and evaluation [24]. The success of the resistive layer indicated that increased resistivity may reduce the spark energy further, however the carbon-epoxy mixtures used so far cannot be made homogeneously at surface resistivity values $>20\text{M}\Omega/\text{square}$. Therefore we proposed to use the highly-resistive materials from the RPC community to explore their potential for spark suppression in combination with our THGEM detectors.

Dixit et al. [77] modeled the diffusion of charge on the resistive layer by assuming Gaussian diffusion. It was observed (also by the Weizmann group [9]), that the resistive layer induces pulses on the primary pad, but also on neighboring pads after a delay (the rate of diffusion was on the order of $\sim 1\text{mm}/\mu\text{s}$). The Dixit model reproduced rather well both the time delay

between the signal on the primary pad and the signal on the neighboring pad, as well as the pulse height ratio between them. However no attempt has been made, to the best of our knowledge, to model the rate dependence of the gain in MPGDs with resistive layers. For this it is necessary to know not just the diffusion of charge, but the fluctuations in the electric field inside the region of multiplication.

As a further evolution, Bashkirov et al. [78] coupled a single-faced THGEM to resistive glass and implemented an ion counter with very high charged avalanches. A similar structure was also suggested in [79] however no results were published to the best of our knowledge. Following this and the previous work described, we implemented the RPC approach by coupling a single-faced THGEM to highly resistive materials of 10^7 - $10^{12}\Omega\text{cm}$. We measured the gain properties, mimicked highly ionizing events, and measured the rate capabilities of this prototype on several materials, with comparison to the THWELL and RWELL.

5.2 Experimental setup and methodology

Our detector was assembled in an aluminum chamber and continuously flushed with 1 atm of Ne/CH₄ (95/5) pre-mixture. The chamber had a 50 μm thick Kapton x-ray window and was irradiated with 8keV x-rays through a 20 μm nickel filter. The configurations used in this work are shown in Figure 23. The induced signal was readout with an Ortec 125 charge sensitive preamplifier connected to an Ortec 570 linear amplifier set to 1 μs shaping time.

5.2.1 Electrode preparation and characteristics

5.2.1.1 Bulk resistivity measurement

The four electrodes (Table 5) were painted with silver paint on both sides—leaving a $\sim 1\text{mm}$ margin. The electrodes were then each sandwiched in between FR4 electrodes with a 2cm diameter circular copper contact (Figure 25) and pressed with a clamp. These connections were connected to a CAEN N471 power supply and from there to a Keithley picoammeter through a 22M Ω resistor. The current was monitored as a function of the voltage. This method was used following [80], however in their work the electrodes were not painted with silver paint, and the temperature and humidity were monitored. Ohmic behavior was observed and the bulk resistivity was calculated using the formula

$$R = \rho \frac{L}{A}, \quad (7)$$

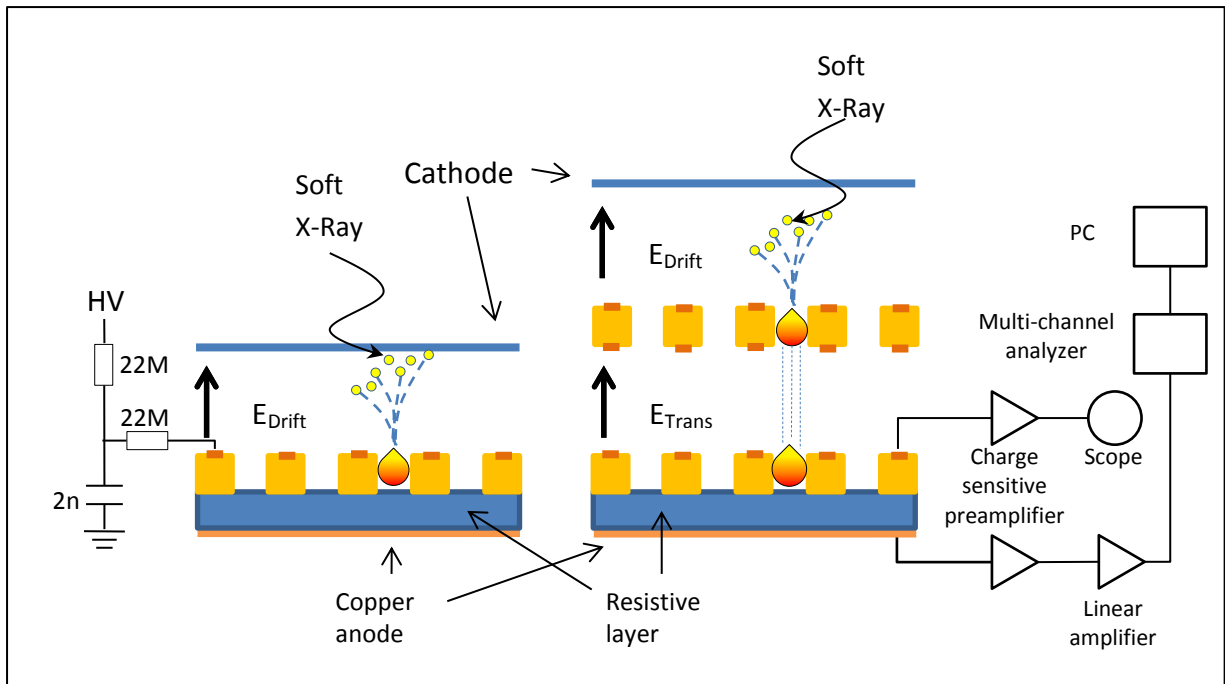


Figure 23: Detector configurations with resistive anodes and readout schemes. WELL configuration (left) is a single-faced THGEM with pitch $a=1\text{mm}$, diameter $d=0.5\text{mm}$, rim $h=0.1\text{mm}$ and thickness $t=0.8\text{mm}$. WELL + charge injector (right) includes a pre-amplification stage with a two-faced THGEM with $a/d/h/t=1/.5/.1/.4\text{mm}$. In both configurations the single-faced THGEM was coupled to a copper anode directly or (as shown here) via a resistive layer. Charges were recorded (as shown on the right scheme) either from the top electrode of the RPWELL or from the bottom electrode coating the resistive plate.

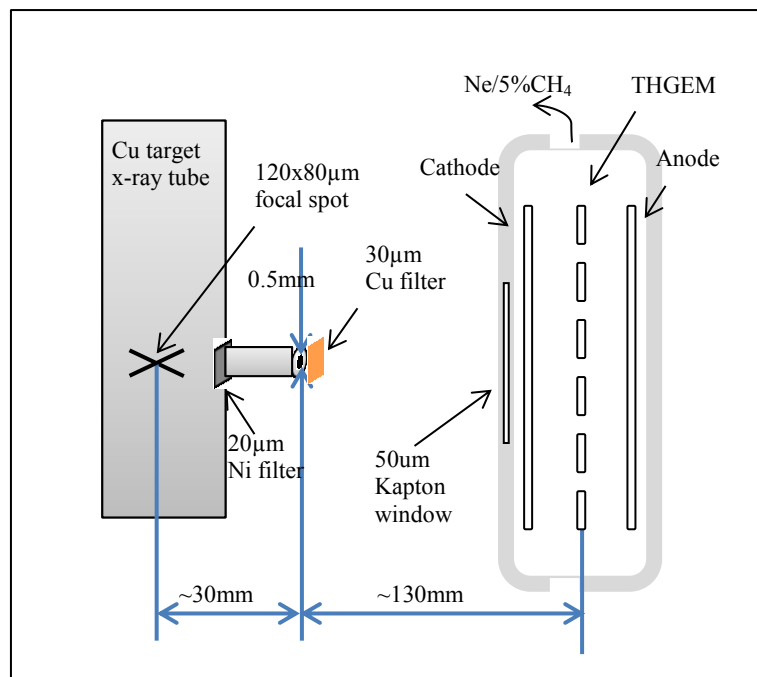


Figure 24: Irradiation setup. The distances were fixed throughout all of the assays. Here the detector is a THGEM with drift and induction gaps.

where R is the resistivity measured, L is the thickness of the material and A is its area. Table 5 summarizes the results.

Table 5: The resistive electrodes used in the experiment.

Electrode	Dimensions [mm]	Bulk resistivity [Ωcm]
VERTEC 400 Glass	36x31x0.4	8×10^{12}
HPL Bakelite	29x29x2	2×10^{10}
Semitron ESD 225	30x30x2	2×10^9
Semitron ESD 225	30x30x4	3×10^9

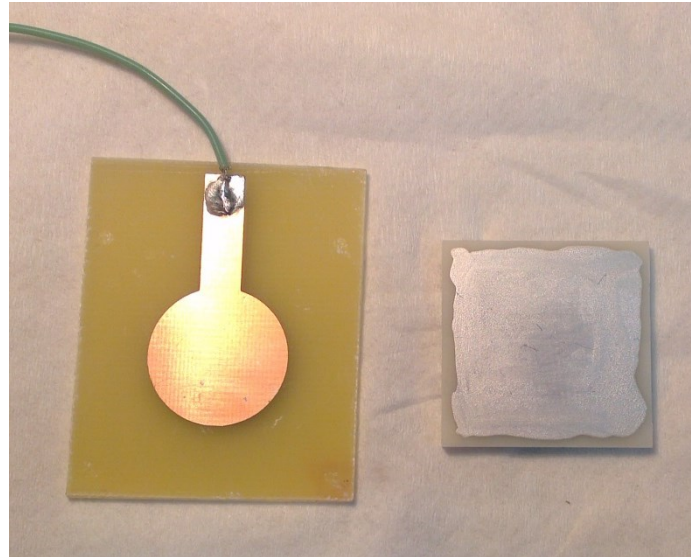


Figure 25: One of the two electrodes (left) used to press the resistive layer (Semitron 2mm) painted with silver paint (right)

5.2.1.2 Electrode preparation

The electrodes were machined to $\sim 30 \times 30 \text{mm}^2$ pieces. These were then painted with silver paint on one side (leaving a $\sim 1 \text{mm}$ margin) and let to dry. Then they were glued with conductive epoxy to copper clad FR4 (Figure 26). The resistive glass had aluminum evaporated onto it and was then glued with conductive epoxy. The difference was due to availability of the evaporation facility and had no visible effect on the contact quality. The $1 \text{M}\Omega/\text{sq}$ resistive layer was prepared by spraying a carbon and epoxy mixture onto a $100 \mu\text{m}$ layer of FR4. It was then biased by using copper tape contact.

5.2.2 Assays

5.2.2.1 Gain curves at different rates

The detector (Figure 23, left) was assembled with a 4mm drift gap, while the x-ray tube was set to 10kV acceleration voltage with a 5mm diameter collimator. Gain curves were taken, keeping $E_{\text{Drift}} = 0.5 \text{kV/cm}$, at rates of roughly $10^{-2} - 10 \text{Hz/mm}^2$. The current to the top electrode was monitored from the CAEN N471 power supply's current monitor (i_{mon}) port via a

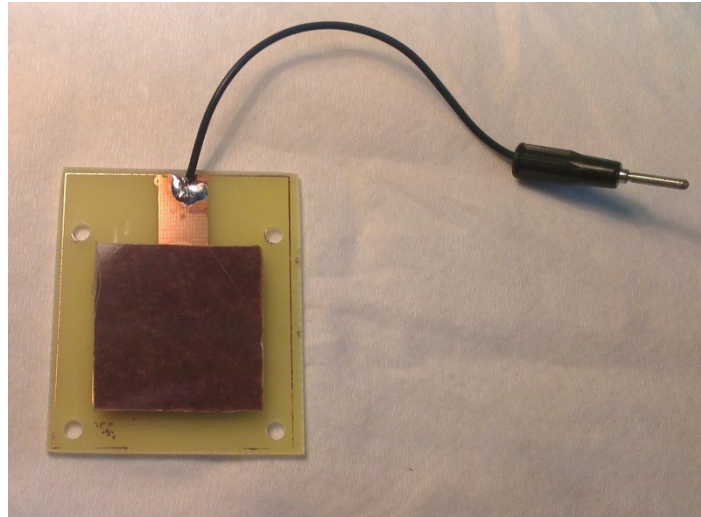


Figure 26: Bakelite resistive layer, painted with silver paint on one side and glued to a copper anode with conductive epoxy.

National Instruments NI-DAQ analog signal digitization board NI-USB 6008. The signal was sampled at 50Hz and recorded using dedicated LabVIEW Signal Express 2012. Sparks were defined as jumps $>30\text{nA}$ in the current.

5.2.2.2 Response to highly ionizing events

In order to test the response of the detector to highly ionizing events we used the “Injector Method” [81]. A pre-amplification THGEM stage was used (Figure 23 right) to enhance the number of the x-ray induced primary electrons and *inject* them into the detector—this is meant to mimic highly ionizing events which deposit a large amount of charge in the conversion volume. There is a certain risk of coupling the two stages to each other; this is examined in the discussion. The detector was assembled with an $a/d/h/t=1/.5/.1/.4\text{mm}$ pre-amplification THGEM stage, using a 5mm drift gap and a 4mm transfer gap with the fields set to $E_{\text{Drift}}=E_{\text{Trans}}=0.5\text{kV/cm}$ (Figure 23 right). Two peaks formed in the recorded spectrum: a high peak due to conversion in the drift gap, multiplied by the injector, and a low peak due to conversion in the transfer gap, multiplied by the WELL (Figure 27). The injector was calibrated by using a THWELL as the bottom stage and setting the detector gain to $\sim 10^3$. Then the injector voltage was raised in 25V steps until the onset of sparks. The injector gain was calculated by taking the ratio of the two peaks formed in the spectrum. Using this method it was possible to take six points in the injector’s gain curve. To measure the higher gains in the injector, the voltage difference across the THWELL was set to zero, and the signal was read out from the top of the single-faced THGEM; similar to a THGEM with an induction gap.

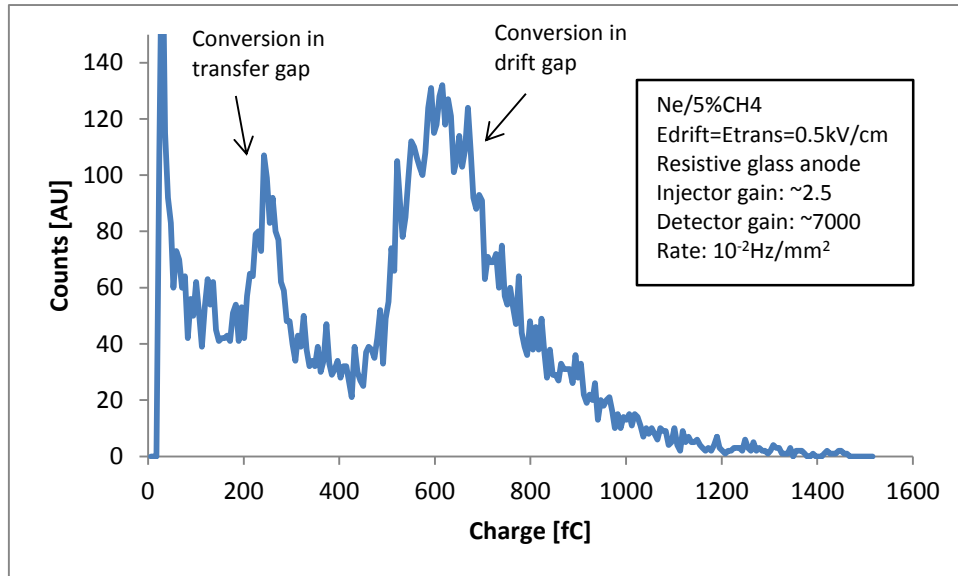


Figure 27: Example spectrum with glass anode and injector (detector shown in Figure 23 right). The two peaks correspond to events multiplied only in the WELL (small charge) and to that pre-amplified by the THGEM injector (large charge).

At the beginning of the measurement the drift voltage was reversed—thus the only signal in the spectrum was that of photons that converted in the transfer gap—and the detector voltage was adjusted to give a gain of ~ 5000 . The drift field was then set back to 0.5kV/cm and the total rate was $\sim 5 \times 10^{-1}\text{Hz/cm}^2$. The injector voltage was increased in 25V steps.

5.2.2.3 Gain dependence on rate

The pre-amplification stage was removed and the detector was assembled (Figure 23, left) with a 10mm drift gap and $E_{\text{Drift}}=0.5\text{kV/cm}$. The x-ray tube was set to 25kV acceleration voltage and the detector was irradiated by a 1mm diameter 8keV x-ray beam. The rate was raised by increasing the current on the x-ray tube, and by removing copper filters from in front of the beam (Figure 24). The gain was estimated by determining the centroid of the spectrum. At the end of each measurement sequence (at $\sim 10^4\text{Hz/mm}^2$), reducing the rate back to the original $\sim 5\text{Hz/mm}^2$ produced a hysteresis, with the gain returning only to 50-75% of the value at the beginning of the measurement. This was the case for the resistive electrodes, as well as for the THWELL detector (with Cu anode). The detector was then left at a rate of 5Hz/mm^2 and spectra were repeatedly recorded. Over the course of 3 hours of low rate irradiation, the WELL detector recovered from 74% of the original gain to 99%. The rate experiment was then repeated, giving similar results. The other electrodes recovered to less than 90% of their original signal, but the full evaluation of these effects requires a broader study—beyond the scope of this work. For the robust detectors (Glass, Bakelite and Semitron

plastic), the experiment was repeated at roughly an order of magnitude higher gains, yielding similar results.

5.3 Results

5.3.1 Pulse shapes and gain curves

Figure 28 shows a comparison of the induced pulses from the detector with different resistive-anode materials (see Table 5); a pulse from a typical THGEM with an induction gap is shown as well. The slower signals of the WELL, relative to the THGEM with induction gap, are due to the ion component present in the WELL geometry, as compared to electron-only signals collected after an induction gap. Figure 29 shows pulse-height spectra acquired at 5×10^3 gain for several materials. The electronic noise—from the amplification chain—was similar in all of the measurements. The resistive materials (particularly the glass, of the highest resistivity) showed higher activity near the low end of the spectrum (between the peak and the electronic noise) compared to the THWELL and RWELL detectors. The resolution was also degraded, with the THWELL, RWELL, RPWELL with 2mm Semitron and RPWELL with glass having resolutions 18%, 20%, 26% and 45% respectively. This is possibly due to recovery effects: the slow recovery time of the resistive materials (~ 2.5 s and 3.5×10^{-4} s for the glass and Semitron respectively) indicates that many primary electrons will enter the hole with a reduced electric field, inducing smaller signals. This naturally will skew the energy distribution to lower values. Careful inspection shows that the energy spectrum with Semitron electrode is not only broader, but slightly skewed to lower values, relative to the THWELL and RWELL spectrums.

Figure 30 shows gain curves acquired with each of the detectors. For the THWELL, RWELL and RPWELL Bakelite detectors the gain curves were terminated by sparks (current pulses > 30 nA). The Glass and Semitron detectors were terminated also due to activity in the current monitor: for the glass, ~ 5 nA pulses of duration 0.02s (1 unit ADC and 1 unit in the time domain) began to appear and became denser at higher voltages; for the Semitron electrodes displayed the same behavior at a ~ 1100 V, at 1125V they shows signals as high as ~ 20 nA of duration 0.02s. The measurements were terminated to prevent damage to the electrodes. It was also observed that lowering the voltage did not restore the original gain, but rather there was a 2-10 fold drop in gain—this was not a permanent drop, as assembling the detector again after several days restored similar gain at the same voltage. In the glass and Bakelite configurations the gain began to saturate at high voltages. This is likely due to the slow

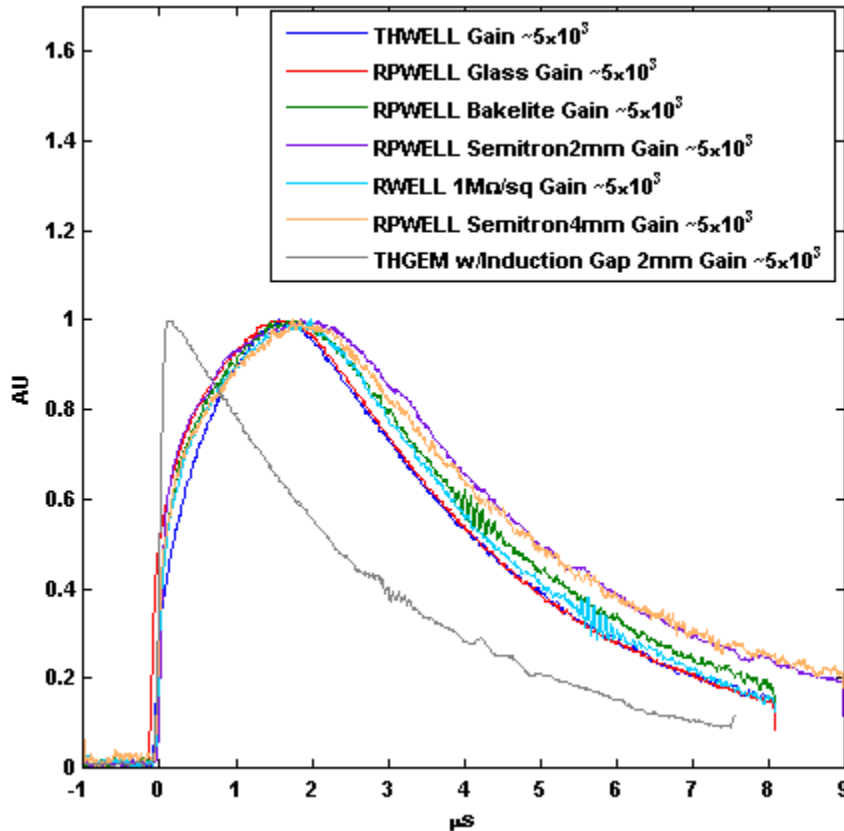


Figure 28: Charge-signals' pulse shapes measured directly from the charge sensitive preamplifier (time constant 4ms) coupled to the anode of the detector (Figure 23, left), with different resistive layers. The signals were measured on a Tektronix TDS3052 digital scope at 50Ω AC coupling (setting a 200kHz lower cutoff on the signal). The signals have been smoothed with a 50 sample moving average filter.

response of the resistive materials. High charged events will temporarily lower the electric field inside the hole until the charge is evacuated. This reduction causes a slower than exponential rise of the gain with voltage as is seen for the Bakelite and Glass electrodes. This also serves to explain why the gain appears to saturate at earlier values as the rate is increased. The Semitron plastics only showed saturation at $\sim 10\text{Hz}/\text{mm}^2$ at a gain of $\sim 3 \times 10^4$, while for the lower rates they did not saturate at the voltage that were explored. In this work we had few samples of the plastics; therefore we terminated the experiments when the current monitor began to show increased activity. Additional study is necessary to determine if and at what gain the electrostatic plastics saturate at varying rates.

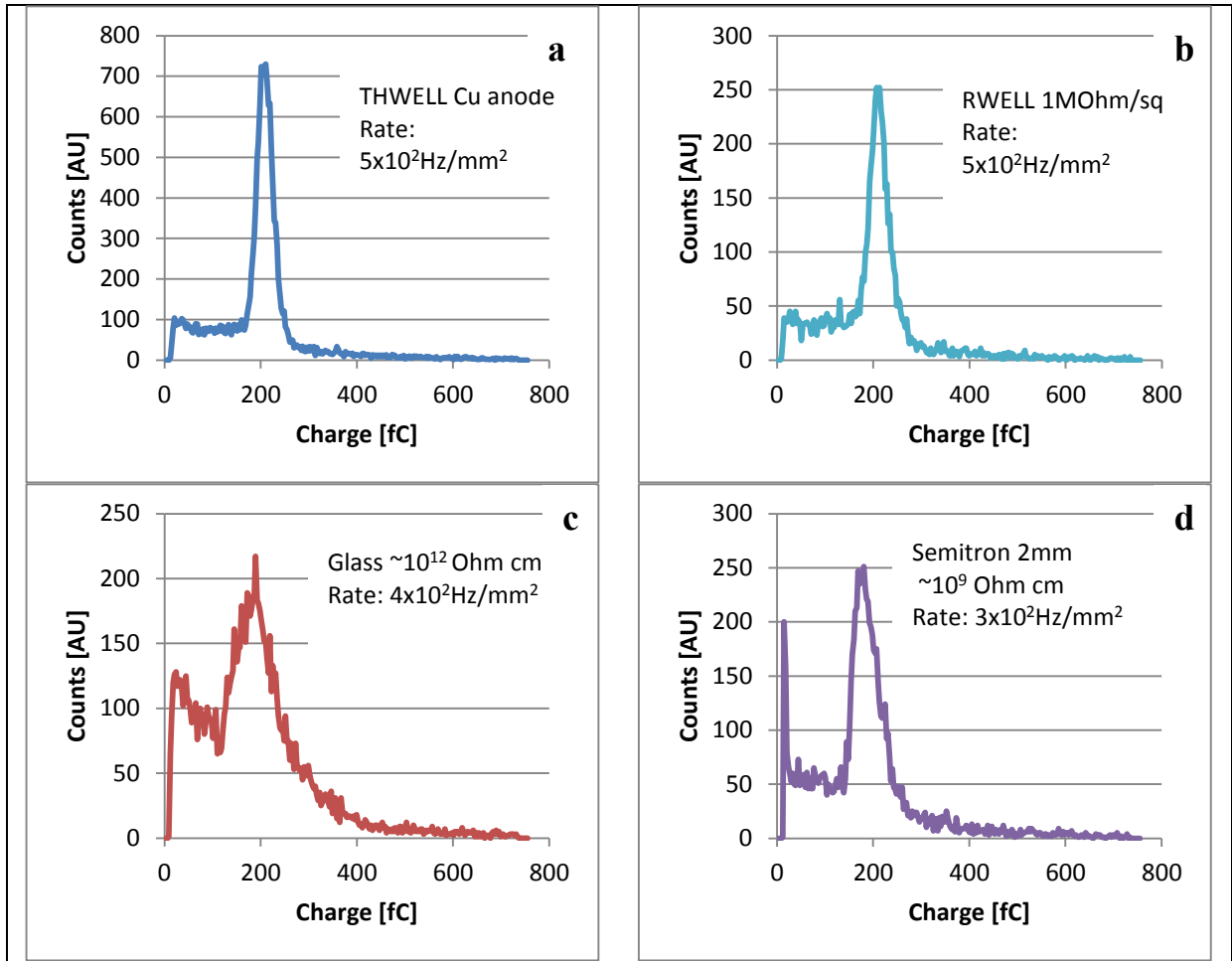


Figure 29: Spectra acquired at a gain of $\sim 5 \times 10^3$ with 8keV x-rays, 10mm drift gap, $E_{\text{Drift}}=0.5\text{kV/cm}$ for: a) THWELL b) RWELL 1M Ω /sq c) RPWELL with glass anode d) RPWELL with Semitron 2mm thick anode.

5.3.2 Exposure to high primary charge

Figure 31 shows the response of the detector to highly ionizing events simulated with the injector (Figure 23, right). The WELL element was kept at a fixed voltage (appropriate for gain of ~ 5000), while varying that of the THGEM-injector. The THWELL and RWELL detectors experienced sparks at injector gains of ~ 36 and ~ 56 respectively. All other electrodes displayed occasional $\sim 5\text{nA}$ current spikes (see Section 5.3.1). Note that the Bakelite electrode did not undergo any sparks. The Semitron electrodes reached 20nA spikes for the highest reached charges. It was also observed that the gain of the WELL detector dropped with increasing the injector gain. This was not a permanent drop: reducing the injector gain restored the original value. The Bakelite performed the worst, dropping nearly

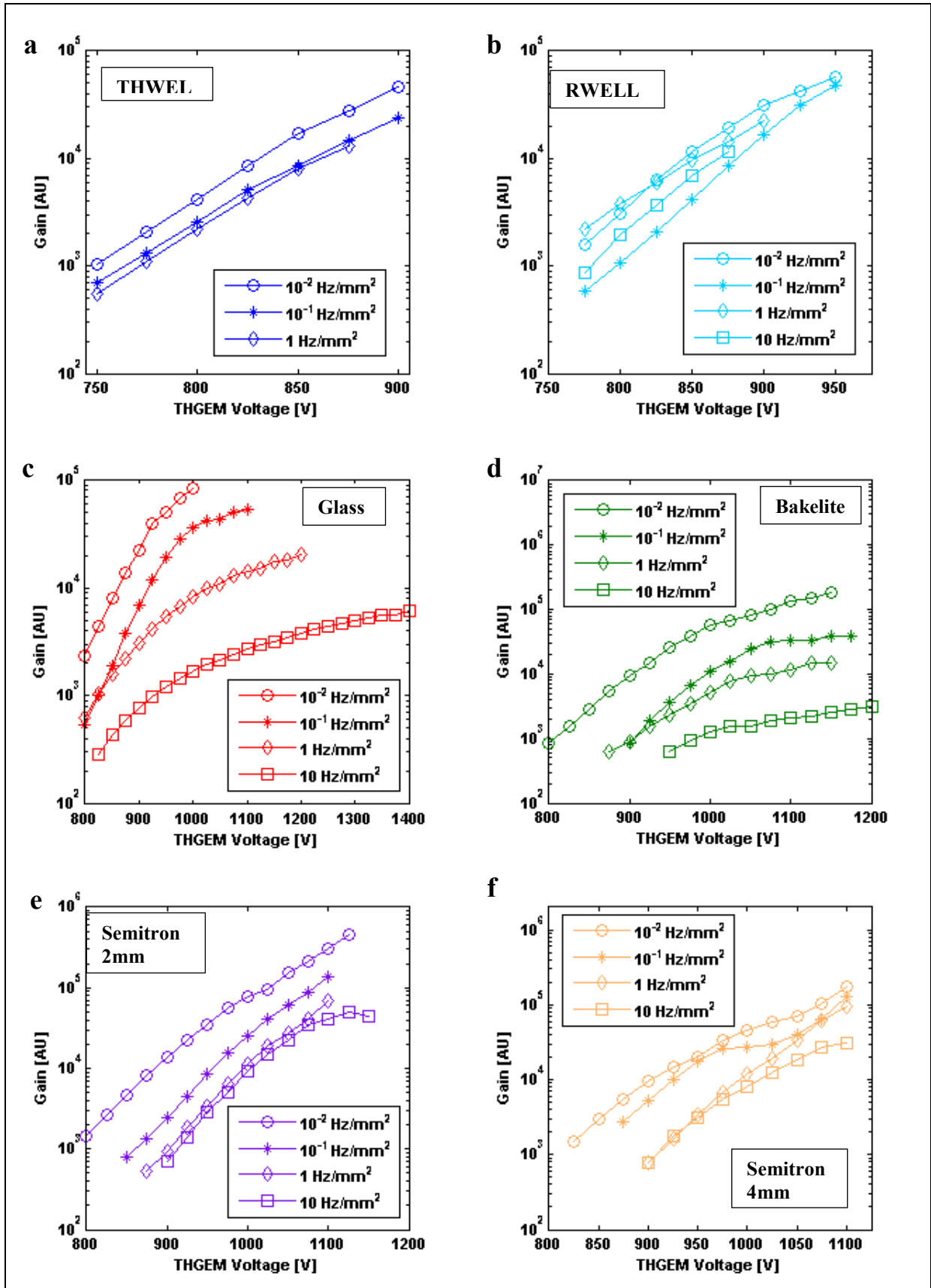


Figure 30: Gain curves taken with 8keV x-rays at $\sim 0.01\text{-}10\text{Hz/mm}^2$ in different WELL-detector configurations with $E_{\text{Drift}}=0.5\text{kV/cm}$ over a 4mm drift gap. The measurements with the THWELL, RWELL and RPWELL-Bakelite detectors were terminated due to the onset of discharges. The RPWELL detectors with the other Glass and Semitron electrodes displayed an enhanced “activity” in the current monitor, but no discharges developed. a) THWELL, b) RWELL 1M Ω /sq, c) Glass, d) Bakelite, e) Semitron 2mm f) Semitron 4mm.

five-fold over an order of magnitude increase in the primary charge. The drop in the WELL detector gain, regardless of electrode, leads us to the conclusion that the single-faced THGEM itself plays a role in lowering the gain, possibly charging up on the bottom insulator. The slope of the THWELL, RWELL and RPWELL with Semitron anode, appear to be very similar, while the anode of highest resistance (Glass and Bakelite) show a steeper decline. This may be due to an additional effect resulting from the slow recovery of the electrode, where the high-charged events do not clear the hole, and cause reduced multiplication for the next event. An experiment to assess this effect would be to repeat the experiment at different rates. This is beyond the scope of this thesis, but is planned for future research.

5.3.3 Rate dependence

The gain dependence on irradiation flux was measured with the detector configuration shown in Figure 23 (left); the gain variation was found to alter between the different anode materials. The Bakelite and Glass RPWELL performed the worst, losing over 90% of their original gain values over a 3 orders of magnitude increase in rate. Both RPWELL detectors with Semitron anodes performed close to the RWELL detector, losing ~60% of their gain over the same rate range. The THGEM with 2mm induction gap was found to be the most robust to rate changes, in agreement with previous results [82]. Note that the assays were limited by the rate capabilities of the MCA—keeping the beam profile constant—and not due to sparks. While the THWELL showed a drop in gain, indicating that the geometry of the THGEM electrode itself may be problematic, charging up on the bottom of the THGEM may explain the slow recovery.

5.4 Discussion on the resistive-anode investigations

We found that reading x-ray induced charges, after multiplication in a WELL detector, through a highly resistive anode gave in most cases spectra well-separated from the noise. The increased proportion of low-amplitude signals for the highly-resistive anode materials are likely due to post-avalanche recovery effects (with many electrons seeing a lower effective electric field). The 2 μ s long rise of the pulses in the WELL configurations (compared to the fast electron signals in THGEMs followed by an induction gap) is due to the avalanche-ion component developing during their evacuation from the holes. While it was later observed that the shaping time of the linear amplifier (1 μ s) was not ideal, subsequent experiments indicated that this caused a difference of 10-15% in the gain, but did not appear to affect the trends presented here—this point is planned to be more fully verified. The gain

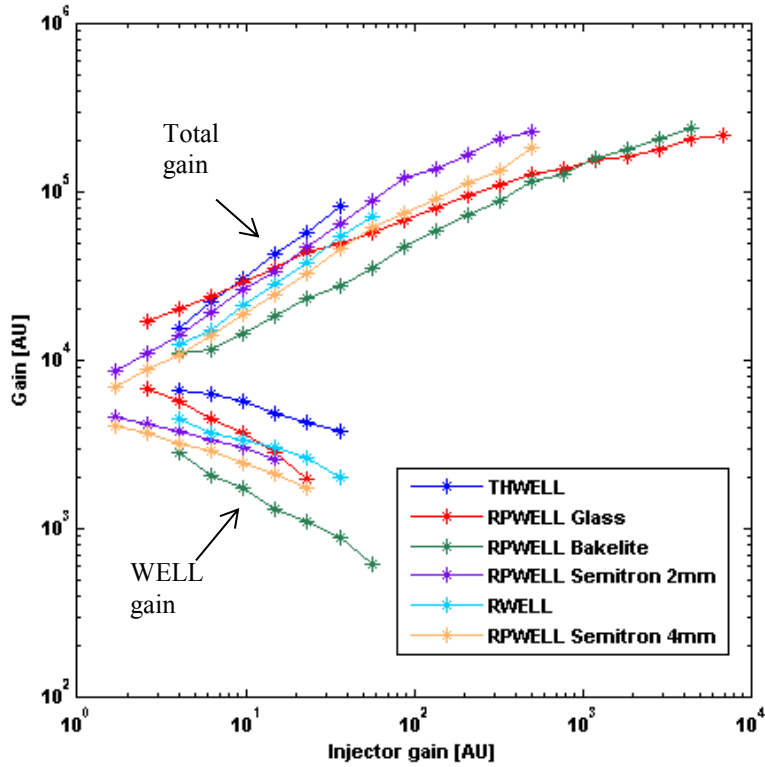


Figure 31: Total gain of the double structure (Figure 23, right) and gain of the WELL (high charge peak and low charge peak in Figure 27 respectively). The gain of the WELL detectors was set to ~ 5000 at the beginning of each measurement. The rate was $\sim 10^{-1}$ Hz/mm², with $E_{\text{Drift}}=E_{\text{Trans}}=0.5\text{kV/cm}$. The measurements were stopped for the THWELL and RWELL detectors due to the onset of sparks. For the RPWELL configurations with bulk resistive anodes, the Glass and Bakelite anode measurements were stopped to prevent discharges in the per-amplification stage (a two-faced THGEM), while the Semitron anode measurements were stopped to protect the material (one current activity was observed in the current monitor).

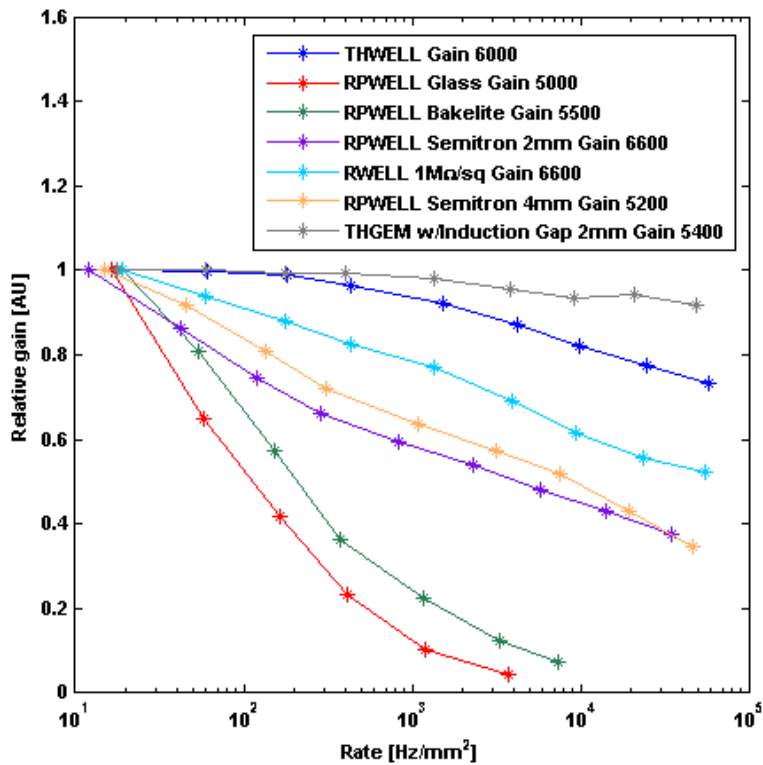


Figure 32: Relative detector gain vs. x-rays rate. The different detector configurations were irradiated with a 1mm diameter 8keV x-ray beam.

curves recorded here (Figure 30) show that coupling WELL structures to these resistive electrodes can yield gains reaching $\sim 10^5$ with a single multiplication stage (Figure 30 c,d,e and f). Some hysteresis effects (pulse-height variations) were not due to permanent damage to the detector and though being of key importance—their study is beyond the scope of this work. Quantities such as humidity and temperature affect the resistivity of the electrodes, but more importantly there are several yet unanswered questions regarding stabilization effects in THGEMs generally [83].

The results with the injector (primary charge multiplier), added to mimic highly ionizing events, showed that the RPWELL configurations with the highly-resistive electrodes are robust relative to the THWELL (with metal anode) and RWELL (with painted $M\Omega/\text{square}$ film). However there are a number of unresolved issues that warrant further study. First, the degree of coupling between the first and second stages (through a transfer gap) is a key factor in determining the interpretation of the results: on the one hand if the transfer gap is too small, the field of the injector may distort that of the THGEM; on the other hand if the transfer gap is too large, diffusion will spread the high primary charge over many holes, making the injected events less similar to realistic HIP events. Additional factors which may influence the results are the collection efficiency of primary charges into the injector holes as well as the fraction of charge collected at the bottom of the injector. In previous work [15] it was shown that for a THGEM with $a/d/t/h=1/.3/.4/.1\text{mm}$ (parameters defined in Figure 1) at a gain of 25, in $\text{Ne}/5\%\text{CH}_4$ the collection efficiency was 100%. However this was in the absence of a drift field. These two issues are related to the degree of coupling between the two stages and require further systematic studies. The RPWELL configurations with highly-resistive electrodes did not spark at gains over a hundred-fold higher (reached with the injector) than in the standard configurations: indicating robust operation in the presence of highly ionizing events (Figure 31). In addition, the drop in gain due to the high primary charge was higher for the electrodes of highest resistivity: Glass and Bakelite (Figure 31), this may be related to rate effects and is discussed below.

The results of the rate-dependence of the pulse-height show that the Semitron polymer has attractive qualities. The rate-induced gain drop of the RWELL with $1M\Omega/\text{sq}$ resistive layer, amounting to $\sim 50\%$ over 3 orders of magnitude increase in rate: from 10 to 10^4 Hz/mm^2 (Figure 32), is similar to what was recently observed with a resistive MICROMEGAS detector [8]. However, measurements of the rate dependence (in “current mode”) with a

0.4mm thick single-faced THGEM with identical parameters and a $10\text{M}\Omega/\text{sq}$ resistive layer (in a RWELL mode) showed a drop of 50% in the gain at a rate of $\sim 10^6\text{Hz}/\text{mm}^2$; this result is about two orders of magnitude better than what was measured in the present work in “counting mode”. We repeated our measurement in “current mode” and found no difference between “current” and “counting” modes. The source of this discrepancy has not been found yet and is the subject of a current study, although it may be related to the quality of the electrode or its thickness (0.8mm in our measurement, 0.4mm in the reference). Note that in previous work [9] $1\text{M}\Omega/\text{sq}$ and $10\text{M}\Omega/\text{sq}$ layers behaved similarly. The Semitron performed only slightly worse than the RWELL (losing 60% over 3 orders of magnitude rates; Figure 32), but conversely it provided a fully spark-free operation and a high dynamic range.

The slow response of the highly resistive layers ($3 \times 10^{-4}\text{s}$ - 2s) can explain both the rate dependence of the gain, and the drop in gain with highly signal events. The field inside the hole depends exponentially on the THGEM voltage difference. Charge that collects at the bottom of the hole on the resistive layer will reduce the field inside the hole, and subsequently reduce the gain. High rate and high charge will cause similar drops in gain, because they affect the rate of accumulation of charge on the layer. Lippmann et al. [73] have calculated field fluctuations on the order of $\sim 8\%$ due to incoming particles at $600\text{Hz}/\text{cm}^2$ for the RPC parallel plate geometry using quasi-static approximation of Maxwell’s equations. Based on the gain curves measured (Figure 30), at a gain of 5×10^3 , a 0.7% drop in the voltage, would cause a 10% drop in gain. The electric fields inside the THGEM hole are on the order of $\sim 10\text{kV}/\text{cm}$. A charge as small as $\sim 10\text{fC}$ distributed uniformly at the bottom of the hole ($\sim 5 \times 10^{-2}\text{mm}^2$), is sufficient to cause a $\sim 1\%$ drop in the field. The balance of charge dispersal (governed by the time constant of the system $\tau = 10^{-4}\text{s} - 1\text{s}$), with the incoming charge could collect charge much greater than that, thus reducing the gain both with rate and charge.

The preliminary measurements presented in this work show that the RPWELL is a promising geometry. The Semitron electrodes are by far the most attractive: showing less noise (Figure 29) relative to the glass anode, better resolution (26% relative to 45% for the glass) and much better rate capabilities (losing only 50% of the gain at $10^4\text{Hz}/\text{mm}^2$, where the glass and Bakelite lost over 90%, Figure 32). This was all done with 100% discharge protection during our measurements; however further testing at higher gains and rates is still necessary.

DHCAL requires a thin detector that can withstand rates on the order of $10\text{Hz}/\text{mm}^2$, the RPWELL with a Semitron electrode performed well within these rate requirements. Although these rates are not in the counting-rate plateau, small shifts in gain are tolerable in a digital sampling device (e.g. in the DHCAL). 2mm thick Semitron electrodes are too thick for digital hadronic calorimetry, requiring the thinnest-possible sampling elements; next in line should be studies of single-faced THGEM electrodes coupled to sub-mm thick Semitron pad anodes. The similar performance of the 2mm and 4mm Semitron electrodes (Figure 30 and Figure 32) suggest adequate performance of the thinner electrodes.

Note that at this point THGEMs in general suffer some gain instabilities which are related to the bare rims etched around each hole (Figure 1), to the electrode's material, to the moisture level etc.; it is therefore difficult to decouple the behavior of a THGEM electrode from the behavior of its resistive anode. However, it is clear that the aim should be to find the least-resistive materials that effectively quench sparks.

6 Summary

Two studies were performed within this thesis work in the field of Thick Gaseous Multipliers (THGEM): the evaluation of avalanche buildup asymmetry inside THGEM holes - applying optical readout, and a systematic investigation of THGEM properties with highly resistive anode materials.

The first study showed that although the avalanche develops asymmetrically inside the hole, there is still a large margin between the avalanche and the edge of the hole. This does not necessarily indicate that the gain limitations due to “surface streamers” hypothesis is invalid; although the majority of avalanches develop far from the edge, perhaps those occasionally occurring near the edge develop into sparks. A broader optical study of spark formation may be possible using a fast (ns) gated image intensifier should be a feasible exciting direction for further research. The tools developed in this study have broader applications; e.g. the asymmetric hole multiplicity could provide means for accurate radiation-impact localization in some basic detector studies and in recording rare events in physics experiments. To our knowledge, this is the first work to study the development of avalanches inside THGEM directly using optical readout.

The second study gave us some direction which may solve—at least for some low-to-medium rate applications—the dynamic range issues of THGEM- based detectors. We investigate a

new structure, the Resistive-Plate WELL (RPWELL), coupling a single-faced THGEM to a bulk resistive anode. Although limited in rate, as shown here, the RPWELL could reach high gains ($\sim 10^5$), still undergoing only low-intensity micro discharges when exposed to highly ionizing background. This tolerance to occasional discharges is important when applying modern high-sensitivity readout electronics. It remains to be seen whether total spark elimination is necessary. Future directions for this technology involve better understanding of both the gain and rate limitations. Among anode resistive materials investigated here, Semitron ESD225 plastic yielded the best performances in terms of rate capabilities. At gains of $\sim 5 \times 10^3$, 50% drop in gain was observed at rates of $\sim 10^4 \text{ Hz/mm}^2$. The rate limits are tolerable in many applications, including sampling elements of DHCAL systems foreseen for the future ILC. Care should be taken though to limit the charge spread along resistive anodes, similarly to anode-segmentation solutions applied in Resistive WELL detectors [9,24,25]. We suggest investigating evaporated pads on the bulk resistive anode as a possible solution.

The robust RPWELL multipliers studied here may become revolutionary detection elements for low rate experiments, providing high dynamic range in the presence of HIP background.

7 References

- [1] F. Sauli, *GEM: A new concept for electron amplification in gas detectors*, *Nucl. Instrum. Meth. A* **386** (1997) 531
- [2] Y. Giomataris, P. Rebourgeard, J. P. Robert, and G. Charpak, *MICROMEGAS: a high-granularity position-sensitive gaseous detector for high particle-flux environments*, *Nucl. Instrum. Meth. A* **376** (1996) 29
- [3] R. Chechik, A. Breskin, C. Shalem, and D. Mörmann, *Thick GEM-like hole multipliers: properties and possible applications*, *Nucl. Instrum. Meth. A* **535** (2004) 303
- [4] H. Nanjo et al., *Neutron sensitivity of thin gap chambers*, *Nucl. Instrum. Meth. A* **543** (2005) 441
- [5] W. Adam et al., *The effect of highly ionising particles on the CMS silicon strip tracker*, *Nucl. Instrum. Meth. A* **543** (2005) 463
- [6] M. Alfonsi et al., *R&D Proposal: Development of Micro-Pattern Gas Detector Technologies*, *CERN Document Server* (2008)
- [7] A. Bressan et al., *High rate behavior and discharge limits in micro-pattern detectors*, *Nucl. Instrum. Meth. A* **424** (1999) 321
- [8] J. Wotschack, *Development of micromegas muon chambers for the ATLAS upgrade*, 2012 *JINST* **7** C02021
- [9] M. Pitt, *Experimental Research in Particle Physics: Detector Development and Data Analysis*, MSc thesis, Weizmann Institute of Science, 2012
- [10] R. Chechik, A. Breskin, and C. Shalem, *Thick GEM-like multipliers—a simple solution for large area UV-RICH detectors*, *Nucl. Instrum. Meth. A* **553** (2005) 35
- [11] M. Cortesi, R. Alon, R. Chechik, A. Breskin, D. Vartsky, and V. Dangendorf, *Investigations of a THGEM-based imaging detector*, 2007 *JINST* **2** P09002
- [12] A. Breskin, *New developments in optical imaging detectors*, *Nucl. Phys. A* **498** (1989) 457
- [13] N. Majumdar, S. Mukhopadhyay, and S. Bhattacharya, *3D field simulation in GEM-type structures*, 2009 *JINST* **4** P10013
- [14] V. Peskov, B. D. Ramsey, and P. Fonte, *Surface streamer breakdown mechanisms in microstrip gas counters*, *Nucl. Instrum. Meth. A* **392** (1997) 89
- [15] C. D. R. Azevedo et al., *Towards THGEM UV-photon detectors for RICH: on single-photon detection efficiency in Ne/CH₄ and Ne/CF₄*, 2010 *JINST* **5** P01002
- [16] M. Alexeev et al., *Detection of single photons with ThickGEM-based counters*, 2012 *JINST* **7** C02014
- [17] S. Duval et al., *Hybrid multi micropattern gaseous photomultiplier for detection of liquid-xenon scintillation*, *Nucl. Instrum. Meth. A* **695** (2012) 163
- [18] A. Breskin et al., *CsI-THGEM gaseous photomultipliers for RICH and noble-liquid detectors*, *Nucl. Instrum. Meth. A* **639** (2011) 117
- [19] ANSYS® Maxwell, *Release 15.0* (2012)
- [20] A. Breskin et al., *A concise review on THGEM detectors*, *Nucl. Instrum. Meth. A* **598** (2009) 107
- [21] M. Cortesi et al., *First studies of electron transport along small gas gaps of novel foil radiation converters for fast-neutron detectors*, 2013 *JINST* **8** P01016
- [22] H. Aihara, P. Burrows, and M. Oreglia, *SiD Letter of Intent*, *arXiv:0911.0006* (2009)
- [23] L. Arazi et al., *THGEM-based detectors for sampling elements in DHCAL: laboratory and beam evaluation*, 2012 *JINST* **7** C05011
- [24] S. Bressler et al., *Beam studies of thin THGEM-based detectors for sampling elements in the DHCAL, In preparation* (2013)

- [25] L. Arazi et al., *Beam studies of the Segmented Resistive WELL: a potential thin sampling element for Digital Hadronic Calorimetry, In Preparation* (2013)
- [26] F. Sauli, *Principles of Operation of Multiwire Proportional and Drift Chambers*, in *Experimental Techniques in High-energy Nuclear and Particle Physics, 2nd Ed*, edited by T. Ferbel, (World Scientific, 1991)
- [27] I. Smirnov, *Interactions of Particles with Gases* (2012)
- [28] R. Veenhof, *Garfield - A Drift-Chamber Simulation Program* (2012)
- [29] M. Cortesi et al., *THGEM operation in Ne and Ne/CH₄*, 2009 *JINST* **4** P08001
- [30] M. J. Berger et al., *XCOM: Photon Cross Section Database*, version 1.5 (National Institute of Standards and Technology, Gaithersburg, MD, 2010)
- [31] J. H. Hubbell and S. M. Seltzer, *Tables of X-Ray Mass Attenuation Coefficients and Mass Energy-Absorption Coefficients*, version 1.4 (National Institute of Standards and Technology, Gaithersburg, MD, 2004)
- [32] E. Nasser, *Fundamentals of Gaseous Ionization and Plasma Electronics* (Wiley-Interscience New York, 1971)
- [33] S. Biagi, *Magboltz - Transport of Electrons in Gas Mixtures* (2012)
- [34] M. Salet and S. C. P. Leite, *Radioluminescence of rare gases*, *Portgal. Phys* **11** (1980) 53
- [35] A. Breskin et al., *A highly efficient low-pressure UV-rich detector with optical avalanche recording*, *Nucl. Instrum. Meth. A* **273** (1988) 798
- [36] A. Pansky, A. Breskin, A. Buzulutskov, R. Chechik, V. Elkind, and J. Va'vra, *The scintillation of CF₄ and its relevance to detection science*, *Nucl. Instrum. Meth. A* **354** (1995) 262
- [37] M. M. F. R. Fraga, F. A. F. Fraga, S. T. G. Fetal, L. M. S. Margato, R. F. Marques, and A. J. P. L. Policarpo, *The GEM scintillation in He-CF₄, Ar-CF₄, Ar-TEA and Xe-TEA mixtures*, *Nucl. Instrum. Meth. A* **504** (2003) 88
- [38] F. Tokanai et al., *Evaluation of a capillary plate gas detector filled with and gas mixtures*, *Nucl. Instrum. Meth. A* **581** (2007) 236
- [39] F. A. F. Fraga, L. M. S. Margato, S. T. G. Fetal, M. M. F. R. Fraga, R. F. Marques, and A. J. P. L. Policarpo, *Luminescence and imaging with gas electron multipliers*, *Nucl. Instrum. Meth. A* **513** (2003) 379
- [40] J. S. E. Townsend, *Electricity in Gases* (Clarendon Press, 1915)
- [41] P. Fonte, V. Peskov, and F. Sauli, *VUV emission and breakdown in parallel-plate chambers*, *Nucl. Instrum. Meth. A* **310** (1991) 140
- [42] M. Alexeev et al., *Ion backflow in thick GEM-based detectors of single photons*, 2013 *JINST* **8** P01021
- [43] H. Raether, *Electron Avalanches and Breakdown in Gases* (Butterworths London, 1964)
- [44] G. F. Knoll, *Radiation Detection and Measurement*, Fourth (John Wiley and Sons, 2010)
- [45] G. D. Alekseev, N. A. Kalinina, V. V. Karpukhin, D. M. Khazins, and V. V. Kruglov, *Investigation of self-quenching streamer discharge in a wire chamber*, *Nucl. Instrum. Meth.* **177** (1980) 385
- [46] A. Oed, *Position-sensitive detector with microstrip anode for electron multiplication with gases*, *Nucl. Instrum. Meth. A* **263** (1988) 351
- [47] A. J. P. L. Policarpo, *The gas proportional scintillation counter*, *Space Science Instrumentation* **3** (1977) 77
- [48] M. Suzuki, P. Strock, F. Sauli, and G. Charpak, *The emission spectra of Ar, Kr and Xe + TEA*, *Nucl. Instrum. Meth. A* **254** (1987) 556

- [49] M. Suzuki et al., *On the optical readout of gas avalanche chambers and its applications*, *Nucl. Instrum. Meth. A* **263** (1988) 237
- [50] M. M. Fraga et al., *Study of scintillation light from microstructure based detectors*, in *1999 IEEE Nuclear Science Symposium, 1999. Conference Record*, (1999), pp. 654 – 659 vol.2
- [51] A. Morozov, L. M. S. Margato, M. M. F. R. Fraga, L. Pereira, and F. A. F. Fraga, *Secondary scintillation in CF₄: emission spectra and photon yields for MSGC and GEM*, 2012 *JINST* **7** P02008
- [52] A. Kaboth et al., *A measurement of photon production in electron avalanches in CF₄*, *Nucl. Instrum. Meth. A* **592** (2008) 63
- [53] F. A. . Fraga et al., *CCD readout of GEM-based neutron detectors*, *Nucl. Instrum. Meth. A* **478** (2002) 357
- [54] A. Roccaro et al., *A background-free direction-sensitive neutron detector*, *Nucl. Instrum. Meth. A* **608** (2009) 305
- [55] M. Gai et al., *An optical readout TPC (O-TPC) for studies in nuclear astrophysics with gamma-ray beams at HIγS*, 2010 *JINST* **5** P12004
- [56] M. Cwiok et al., *Optical time projection chamber for imaging of two-proton decay of ⁴⁵Fe nucleus*, in *2004 IEEE Nuclear Science Symposium Conference Record*, (2004), pp. 1152 – 1156 Vol. 2
- [57] P. K. Lightfoot, G. J. Barker, K. Mavrokoridis, Y. A. Ramachers, and N. J. C. Spooner, *Optical readout tracking detector concept using secondary scintillation from liquid argon generated by a thick gas electron multiplier*, 2009 *JINST* **4** P04002
- [58] A. Bondar et al., *On the low-temperature performances of THGEM and THGEM/G-APD multipliers in gaseous and two-phase Xe*, 2011 *JINST* **6** P07008
- [59] *Matlab R2012a* (Mathworks, 2012)
- [60] *ANSYS® Academic Research, Release 13.0* (2012)
- [61] R. Santonico and R. Cardarelli, *Development of resistive plate counters*, *Nucl. Instrum. Meth. in Physics Research* **187** (1981) 377
- [62] G. Carlino et al., *The ATLAS RPC Level-1 muon trigger: design and simulation*, *Nucl. Instrum. Meth. A* **533** (2004) 188
- [63] A. Zallo, *The BaBar RPC system*, *Nucl. Instrum. Meth. A* **456** (2000) 117
- [64] S. Ramo, *Currents Induced by Electron Motion*, *Proceedings of the IRE* **27** (Sept.) 584
- [65] R. Cardarelli, R. Santonico, A. Di Biagio, and A. Lucci, *Progress in resistive plate counters*, *Nucl. Instrum. Meth. A* **263** (1988) 20
- [66] I. Duerdoth et al., *The transition from proportional to streamer mode in a resistive plate chamber*, *Nucl. Instrum. Meth. A* **348** (1994) 303
- [67] R. Cardarelli, V. Makeev, and R. Santonico, *Avalanche and streamer mode operation of resistive plate chambers*, *Nucl. Instrum. Meth. A* **382** (1996) 470
- [68] E. Iarocci, *Plastic streamer tubes and their applications in high energy physics*, *Nucl. Instrum. Meth. in Physics Research* **217** (1983) 30
- [69] D. Gonzalez-Diaz and A. Sharma, *Current Challenges and Perspectives in Resistive Gaseous Detectors: a manifesto from RPC 2012*, *arXiv:1206.2735* (2012)
- [70] L. Naumann, R. Kotte, D. Stach, and J. Wüstenfeld, *Ceramics high rate timing RPC*, *Nucl. Instrum. Meth. A* **628** (2011) 138
- [71] A. L. Garcia et al., *Extreme high-rate capable timing resistive plate chambers with ceramic electrodes*, 2012 *JINST* **7** P10012
- [72] M. Abbrescia, *The dynamic behaviour of Resistive Plate Chambers*, *Nucl. Instrum. Meth. A* **533** (2004) 7
- [73] C. Lippmann, W. Riegler, and A. Kalweit, *Rate effects in resistive plate chambers*, *Nuclear Physics B - Proceedings Supplements* **158** (2006) 127

- [74] T. Alexopoulos et al., *A spark-resistant bulk-micromegas chamber for high-rate applications*, *Nucl. Instrum. Meth. A* **640** (2011) 110
- [75] P. Fonte, P. Martinengo, E. Nappi, R. Oliveira, and V. Peskov, *Progress in developing hybrid RPC: GEM-like detectors with resistive electrodes*, *Nucl. Instrum. Meth. A* **602** (2009) 850
- [76] A. Ochi, Y. Homma, H. Komai, Y. Edo, T. Yamaguchi, and R. de Oliveira, *Development of Micro Pixel Chamber with resistive electrodes*, 2012 *JINST* **7** C05005
- [77] M. S. Dixit and A. Rankin, *Simulating the charge dispersion phenomena in Micro Pattern Gas Detectors with a resistive anode*, *Nucl. Instrum. Meth. A* **566** (2006) 281
- [78] V. A. Bashkirov, R. F. Hurley, and R. W. Schulte, *A novel detector for 2D ion detection in low-pressure gas and its applications*, in *2009 IEEE Nuclear Science Symposium Conference Record (NSS/MIC)*, (IEEE, 2009), pp. 694–698
- [79] A. Di Mauro et al., *A New GEM-like Imaging Detector with Electrodes Coated with Resistive Layers*, in *IEEE Nuclear Science Symposium Conference Record, 2006*, (2006), pp. 3852–3859
- [80] K. K. Meghna et al., *Measurement of electrical properties of electrode materials for the bakelite Resistive Plate Chambers*, *arXiv:1206.5894* (2012)
- [81] L. Moleri, *Dynamic Range Optimization of THick Gas Electron Multipliers*, MSc thesis, Universita degli Studi di Milano, 2012
- [82] V. Peskov, M. Cortesi, R. Chechik, and A. Breskin, *Further evaluation of a THGEM UV-photon detector for RICH – comparison with MWPC*, 2010 *JINST* **5** P11004
- [83] R. Chechik, M. Cortesi, A. Breskin, D. Vartsky, D. Bar, and V. Dangendorf, *Thick GEM-like (THGEM) detectors and their possible applications*, in *SNIC Symposium*, (Stanford, California, 2006)